

EFFECTIVE KAON-NUCLEON CROSS SECTION FROM NUCLEAR
TRANSPARENCY MEASURED IN THE $A(E, E'K^+)$ REACTION

By

Nuruzzaman

A Thesis Dissertation
Submitted to the Faculty of
Mississippi State University
in Partial Fulfillment of the Requirements
for the Degree of Master of Science
in Physics
in the Department of Physics and Astronomy

Mississippi State, Mississippi

August 2010

Copyright by

Nuruzzaman

2010

EFFECTIVE KAON-NUCLEON CROSS SECTION FROM NUCLEAR
TRANSPARENCY MEASURED IN THE $A(E, E'K^+)$ REACTION

By

Nuruzzaman

Approved:

Dipankar Dutta
Assistant Professor of Department
of Physics and Astronomy
(Major Professor)

James A. Dunne
Professor of Department
of Physics and Astronomy
(Committee Member)

David L. Monts
Professor of Department
of Physics and Astronomy
and Graduate Coordinator
(Committee Member)

Gary Myers
Dean of Arts and Sciences

Name: Nuruzzaman

Date of Degree: August 7, 2010

Institution: Mississippi State University

Major Field: Physics

Major Professor: Dr. Dipankar Dutta

Title of Study: EFFECTIVE KAON-NUCLEON CROSS SECTION FROM NUCLEAR TRANSPARENCY MEASURED IN THE $A(E, E'K^+)$ REACTION

Pages in Study: 86

Candidate for Degree of Master of Science

Hadron propagation in the nuclear medium is essential for building an accurate model of the nuclear many-body system. Quasi-free electron scattering from nuclei is one of the tools used in the study of hadron propagation effects in the nuclear medium. Electroproduction and propagation of kaons from nuclei provides an additional (strangeness) degree of freedom, inaccessible with other hadrons. An experiment to measure the transparency of pions was completed in Dec 2004 at the Thomas Jefferson National Accelerator Facility in Hall C. Using same data set, we report the first measurement of the nuclear transparency of kaons for ^{12}C , ^{63}Cu and ^{197}Au nuclei at $Q^2 = 1.1, 2.0$ and 3.0 (GeV/c)^2 . We have also extracted the average effective kaon-nucleus cross section from the nuclear transparency. The Q^2 and A dependence of the transparency and average effective cross section are compared to results from kaon-nucleus scattering data and found consistent within experimental uncertainties.

DEDICATION

To my parents Md. Shamsuzzoha, Nurun Nahar and my sister Arjun Nahar and my
dearest friend Shampa Samanta,

And

My teacher Probodh Mondal, Malay Dutta, Subroto Kundu and Dipangkar Dutta

ACKNOWLEDGMENTS

This experiment was sponsored by the Department of Energy Office of Science Grant No.: DE-FG02-07ER41528. I am very grateful for the support I received and the opportunities that were available during this time. I am indebted to seemingly countless people for what I have accomplished and, first of all, I would like to say thank you to all of these people.

My supervisor, Dr. Dipangkar Dutta, provided me with many opportunities and I am deeply grateful for his support through the entire process. When I first joined the Mississippi State University graduate program, Dr. Dutta welcomed me to his research group and explained all the opportunities I can have. He provided many interesting projects to work on, including the nuclear transparency of kaons and weak charge measurement of protons at Jefferson Lab. He encouraged me to attend several conferences during my years at MSU, including those in Mexico, St. Louis, Atlanta, California and Washington APS conferences. He went above and beyond in giving me support and encouragement, particularly during the times before meetings and conferences. He was a spokesperson for the experiment in this thesis and he tirelessly answered many questions which I had about the analysis of the experiment.

During the three years stay at MSU, I had a wonderful experience with our medium energy physics group. Dr. James Dune, along with Dr. Dipangkar Dutta, helped me a

lot. My colleagues in the group Amrendra Narayan, Luwani Ndukum, Adesh Subedi, Jed Leggett and Azmi al Masalha also extended their helping hands all the time. Special thanks to Amrendra Narayan for his enormous help and support. He was with me always in my ups and downs.

I can't thank enough to my closest friends in the department, Saurabh Dayal, Nimisha Srivastava, Markandey Tripathi, Peeyush Sahay, Hazem Abusura, Chandrasiri Ihalawela, and Ruiyuan Mu for their support throughout.

Also, I want to thank my committee members who read and provided useful feedback on this thesis: Dipangkar Dutta, James A. Dune and David L. Monts.

A special thanks goes to my roommate, Jonathan Miller, who was been with me through my MS thesis. There are not words to describe the importance of our friendship. John has been there with me in the best and worst of times.

I'd also like to specially thanks my friends in the department, Jarrod Marsh, Katja Schaefer, Charles Vaughan, Krishna Kanth Ayyalasomayajula, Quarat Ul-Ann Ijaz, Xin Li, Jie Shu, Sergey Ilyushkin, Jeong Pil Song, and Laalitha Liyanage for all of their support and friendship over the years and because they have become an extended family for me.

I would like to thank my seniors, Vidhu Tiwari and Amitava Moitra, in the department for their help on so many occasions.

TABLE OF CONTENTS

DEDICATION	ii
ACKNOWLEDGMENTS	iii
LIST OF TABLES	viii
LIST OF FIGURES	ix
LIST OF SYMBOLS, ABBREVIATIONS, AND NOMENCLATURE	xi
CHAPTER	
1. INTRODUCTION	1
1.1 Experimental Motivation	1
1.2 Nuclear Transparency	3
1.3 Previous Measurements	3
1.4 Experimental Background	4
1.5 Kinematics	4
2. EXPERIMENTAL APPRATUS	8
2.1 TJNAF Overview	8
2.2 Accelerator	8
2.2.1 Polarized Source	10
2.2.2 LINAC	10
2.3 Beamline	12
2.3.1 Hall-C Beamline	12
2.3.2 Beam Position Monitor	12
2.3.3 Beam Current Monitor	12
2.3.4 Raster	13
2.4 Hall-C	13
2.4.1 Short Orbit Spectrometer (SOS)	14
2.4.2 High Momentum Spectrometer (HMS)	14
2.4.3 Target	15

2.4.4	Detector Packages	15
2.5	Data Acquisition	17
2.6	Kinematic Settings	17
3.	MONTE CARLO SIMULATION	19
3.1	General Overview	19
3.2	Ingredients of SIMC	19
3.2.1	Event Generation	19
3.2.2	Spectrometer Simulation	20
3.2.3	Physics Model	21
3.2.4	Kaon Decay	22
3.2.5	Spectral Function	23
3.3	Comparison of Data with SIMC	23
4.	ANALYSIS	27
4.1	General Overview	27
4.2	Particle Identification(PID)	28
4.2.1	Tracking	28
4.2.2	Charge-Normalized Yield	28
4.2.3	Coincidence Time	29
4.2.4	Missing Mass	32
4.2.5	Čerenkov Radiation	37
4.3	Cuts	40
4.3.1	Other Cuts	41
4.4	Comparison of Data with SIMC Yields	42
5.	RESULTS	48
5.1	Transparency	48
5.1.1	Transparency with Respect to Deuterium	49
5.2	Error Calculation	49
5.2.1	Statistical Error Calculation	51
5.2.2	Systematic Error Calculation	52
5.3	Effective Cross Section	53
5.3.1	Effective Cross Section of Kaons(K^+)	54
5.3.2	Effective Cross Section of Pions (π^+)	56
5.3.3	Effective Cross Section of Protons (p)	56
5.3.4	Effective Cross Section for All Hadrons (π^+ , K^+ , p)	59
5.3.5	A Dependency of Transparency	63
6.	CONCLUSIONS	66

6.1	Conclusions	66
6.2	Further Research	67
REFERENCES		68
APPENDIX		
A.	TRANSPARENCY WITH HYDROGEN	72
A.1	Transparency with Respect to Hydrogen	73
B.	MISCELLANEOUS	76
B.1	α Plot	77
B.2	Comparison of Yields for Data with SIMC	77
B.3	Iteration	83

LIST OF TABLES

2.1	The central kinematics of the experiment.	18
4.1	Cuts applied on the reconstructed variables for data or SIMC	41
5.1	T and σ_{eff} for different targets with respect to LD_2	51
5.2	Systematic Error.	52
5.3	Effective cross section for different targets and of Q^2 for kaons	54
5.4	Average effective cross section for different Q^2 for kaons.	56
5.5	Effective cross section for different targets and of Q^2 for pion.	57
5.6	Average effective cross section for different Q^2 for pion.	57
5.7	Average effective cross section for different T_K for protons[17].	59
5.8	Scale factors for different hadron-nucleon scattering.	60
5.9	α values for different Q^2 for kaons with respect to LD_2	63
A.1	Cross section for hydrogen for different Q^2 for kaons.	73
A.2	T and σ_{eff} for different targets with respect to H_2	75
A.3	Cross section for deuterium for different Q^2 for kaons.	75
B.1	α values for different Q^2 for kaons with respect to hydrogen.	77

LIST OF FIGURES

1.1	The schematic kaon electro-production reaction.	5
2.1	Aerial view of Jefferson Lab [18].	9
2.2	Schematic of Jefferson Lab.	11
2.3	Hall C at Jefferson Lab.	13
2.4	Side view of SOS [11].	14
2.5	Side view of HMS [11].	15
2.6	Schematic diagram of target ladder [3].	16
3.1	Schematic of kaon electro-production from a proton.	21
3.2	Schematic of kaon electro-production from different targets.	22
3.3	HMS reconstructed angles and momentum fraction.	25
3.4	SOS reconstructed angles and momentum fraction.	26
4.1	Coincidence time plot of the experiment.	30
4.2	Zoomed coincidence time plot of the experiment.	31
4.3	One-dimensional missing mass plot.	34
4.4	One-dimensional missing mass plot after applying cuts.	35
4.5	Two-dimensional plot of missing mass vs coincidence time.	36
4.6	Aerogel Čerenkov detector.	38
4.7	Gas Čerenkov detector.	39

4.8	Comparison of Q^2 from data and SIMC.	43
4.9	Comparison of Q^2 from data and SIMC.	44
4.10	Comparison of W from data and SIMC.	45
4.11	Comparison of t from data and SIMC.	46
4.12	Comparison of ϕ_{pq} from data and SIMC.	47
5.1	Nuclear transparency for targets of $A > 2$ with respect to LD_2	50
5.2	Effective cross section comparison.	55
5.3	Effective cross section vs transparency.	58
5.4	Hadron-proton total cross section vs T_{hadron}	61
5.5	Comparison of effective and hadron-proton total cross section.	62
5.6	α from electro-production of hadrons and from hadron-scattering.	64
A.1	Nuclear transparency with respect to H_2 target.	74
B.1	α for different kinematics electro-production and hadro-production.	78
B.2	Missing mass are shown here after applying cuts.	79
B.3	Comparison of W from data and SIMC.	80
B.4	Comparison of t from data and SIMC.	81
B.5	Comparison of ϕ^{pq} from data and SIMC.	82
B.6	Fitting Q^2 for iteration.	84
B.7	Fitting W for iteration.	85
B.8	Fitting t for iteration.	86

LIST OF SYMBOLS, ABBREVIATIONS, AND NOMENCLATURE

TJNAF Thomas Jefferson National Accelerator Facility

JLAB Jefferson Lab

CEBAF Continuous Electron Beam Accelerator Facility

linac linear accelerator

SOS Short Orbit Spectrometer

HMS High Momentum Spectrometer

SIMC Simulation Monte Carlo for Hall-C

CODA CEBAF Online Data Acquisition

ROC Read Out Controller

CPU Central Processing Unit

EPICS Experimental Physics Industrial Control System

MC Monte Carlo

BCM Beam Current Monitor

BPM Beam Position Monitor

ns nanosecond

mC millicoulomb

mb millibarn

ADC analog to digital converter

TDC time to digital converter

atm atmosphere (unit)

C.M. Center of Mass

L-T longitudinal-transverse
 K^+ kaons
 π^+ pions
 N nucleon
 p proton
 e electron
 e' scattered electron
 LD_2 Liquid Deuterium
C Carbon
Cu Copper
Au Gold
Al Aluminum
 Q^2 four momentum transfers square
 W center of mass energy
 t four momentum transfer in center of mass system
 ϕ_{pq} angle between reaction plane and scattering plane
 P_{hadron} momentum of the hadron(p, π^+, K^+)
 A mass number of the nucleus
 Z number of protons in the nucleus
 T transparency
 \bar{Y} yield
 σ cross section
 σ_{eff} effective cross section
 M_Λ missing mass of particle Λ
 M_Σ missing mass of particle Σ
 T_K kinetic energy
GeV giga electron volt
MeV mega electron volt

CHAPTER 1

INTRODUCTION

1.1 Experimental Motivation

The propagation of hadrons in the nuclear medium is an essential element of the nuclear many-body problem, which seeks to better understand how to construct the many-body nuclear system from the more basic meson-nucleon and nucleon-nucleon amplitudes. Quasi-free electron scattering from nuclei provides an excellent tool for a microscopic examination of hadron propagation effects in the nuclear medium. The relative weakness of electromagnetic probe and very well understood interaction at the production vertex are some of the well known advantages of electron scattering. Hence, quasi-free production can be viewed as tagging a source of hadrons emerging from throughout the nuclear volume, with minimal disruption of the system. Thus over the past two decades, proton propagation in nuclei has been studied extensively using quasi-free electron scattering [16, 23, 26, 1, 17]. Recently, pion propagation in nuclei has also been studied using exclusive electroproduction of pions from nuclei [10, 28].

Electro-production¹ of K^+ from nuclei provides an additional (strangeness) degree of freedom, which is inaccessible with nucleons and pions. Strangeness provides a unique window on the nuclear many-body problem via access to energy levels that protons and

¹Electron scattering reaction, where electrons are used as a probe.

neutrons cannot occupy. Moreover, the K^+ -nucleon ($K^+ - N$) interaction is relatively weak and varies smoothly with energy [12], which makes them ideal for studying the K^+ -nucleus interaction, as well as the physics of hadron formation. Typically, the K^+ -nucleus interaction has been studied using K^+ scattering from nuclear targets, and these experiments can be considered as analogous to electron scattering since both involve weakly interacting probes.

In spite of the $K^+ - N$ interaction being relatively weak and free of resonance structure, it is difficult to build a description of the kaon-nuclear scattering from the elementary $K^+ - N$ interaction [32]. Differential and total cross section measurements [5, 25, 24, 30, 33] from K^+ scattering experiments show significant discrepancy when they are compared to theoretical calculations [32, 9, 27, 31]. Even in experiments where the ratio of total cross section for a nuclear target to that for a deuteron is measured [5, 25, 24, 30, 30, 33], where the theoretical uncertainties are expected to cancel in the ratio, the theoretical results are found to be systematically smaller than the data [32, 9, 27, 31].

As conventional nuclear physics models have failed to account for the data, several exotic mechanisms have been proposed by various authors [21]. These include modification of the nucleon size in the nuclear medium [32], reduced meson masses in the nuclear medium [4], meson exchange currents [2, 20], long range correlations [15], and various other mechanisms [7].

1.2 Nuclear Transparency

The electro-production of kaons from nuclei is an excellent alternative to the kaon-nucleus scattering in order to extract nuclear transparency. Nuclear transparency is defined as the ratio of the cross section per nucleon for a process on a bound nucleon in the nucleus to the cross section for the process on a free nucleon [13]. One can parametrize the hadron nucleus cross section as $\sigma_N = \sigma_0 A^\alpha$, where σ_0 is the N-N cross section in free space. Then nuclear transparency can thus be parametrized as $T = A^{(1-\alpha)}$. In other words, nuclear transparency can be interpreted as the probability that the hadron produced in the reaction is not scattered outside of the experimental acceptance by the residual nucleus.

1.3 Previous Measurements

There were several experiments performed in last decade at Thomas Jefferson National Accelerator Facility (Jefferson Lab) to measure the transparency of kaons from different processes. The study of $(e, e' K^+)^2$ on carbon and aluminum were performed in Jefferson Lab during 2001. The quasi-free production of the Λ , Σ^0 and Σ^- hyperons was studied in the reaction. An A dependence of effective nucleon number was analyzed and the cross section was also fitted to a power law [34]. Another experiment E93-018 at Jefferson Lab was performed to measure kaon electro-production on hydrogen in two hyperon channels $(e, e' K^+) \Lambda$ and $(e, e' K^+) \Sigma$. This data was taken for $Q^2 = 0.52, 0.75, 1.00$ and 2.00 (GeV/c)² in this experiment. Cross sections averaged over the azimuthal angle were extracted at each of these twelve points for each hyperon. Rosenbluth separations were

²Reaction represents electron scattering from nucleon or nuclear target with final product as scattered electron and kaon.

performed to separate the longitudinal and transverse production cross sections [29]. The quasi-elastic $(e, e'p)$ reaction was studied on targets of deuterium, carbon, and iron up to a value of momentum transfer Q^2 of 8.1 (GeV/c)^2 at Jefferson Lab. A nuclear transparency was determined by comparing the data to calculations in the experiment. The dependence of the nuclear transparency on Q^2 and the mass number A was investigated [17].

1.4 Experimental Background

The electro-production of kaons from nuclei is an excellent alternative to the kaon-nucleus scattering in order to explore the propagation of kaons through the nuclear medium. It may help to resolve discrepancies between theory and experiment which are related to the details of the reaction mechanism or due to the various approximations made in calculating the cross sections. In this analysis, we report the first measurement of the nucleon number, A , and Q^2 dependences of nuclear transparency for the $A(e, e'K^+)$ process. The measurement was performed on ^2H , ^{12}C , ^{27}Al , ^{63}Cu and ^{197}Au nuclei over a Q^2 range of 1.1 to 3.0 (GeV/c)^2 .

1.5 Kinematics

The basic reaction studied for the experiment can be written as

$$e + A \rightarrow e' + K^+ + X \quad (1.1)$$

where X represents other particles in the final state (for example, a neutron and the residual $A - 1$ nucleons). A schematic of the reaction is shown in Figure 1.1. The variables

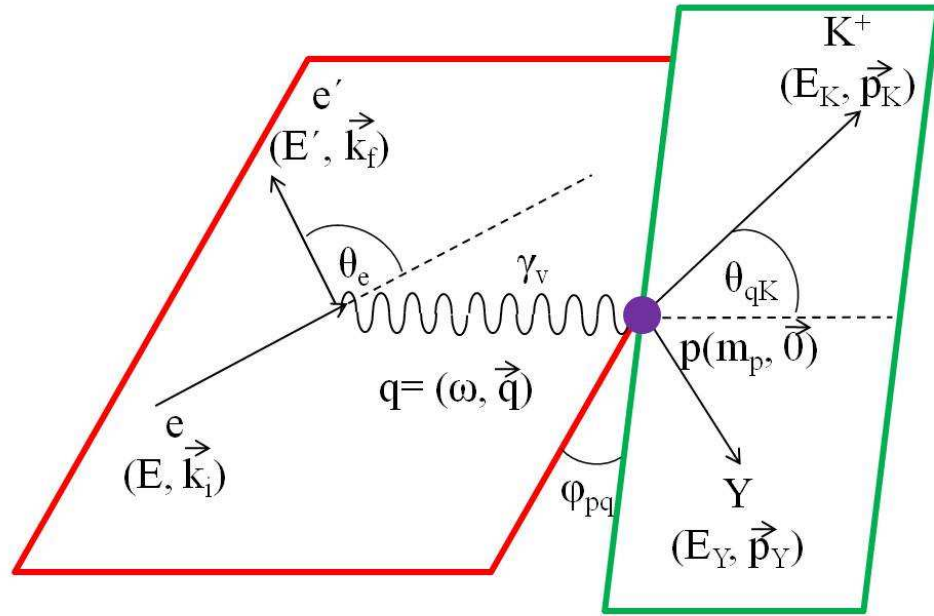


Figure 1.1 The schematic kaon electro-production reaction.

The azimuthal angle between the scattering and reaction planes with respect to the direction of the virtual photon.

are defined in the lab frame. The scattering plane is the plane which contains the three-momentum of the incident and scattered electron and the reaction plane is the plane which contains momentum of virtual photon(\vec{q}) and the kaon momentum vector. θ_e is the electron scattering angle and θ_{pq} is the angle between the three-momentum of the virtual photon and the kaon. ϕ_{pq} is the angle between the scattering plane and the reaction plane.

The kaon electro-production cross section can be expressed as a function of Q^2 , W and t , where $q^2 = -Q^2$ is the four-momentum transfer squared and W is the invariant mass of the virtual photon and the target, given by

$$Q^2 = 4EE' \sin^2(\theta/2) \quad (1.2)$$

$$W = \sqrt{M_A^2 + 2M_A\omega - Q^2} \quad (1.3)$$

where ω (also called ν) is the energy of the virtual photon $= E - E'$ in lab frame. E is energy of incident electron and E' is that of the scattered electron. The four-momentum square of the momentum transferred to the nucleon(s), t , is given by

$$t = (q - p_K)^2 = (E_K - \omega)^2 - |P_K|^2 - |q|^2 + 2|P_K||q|\cos(\theta_{pq}) \quad (1.4)$$

here P_K and E_K are the momentum and energy of the kaon, respectively.

The different hyperons produced in the reaction, shown in Figure 1.1(described in Section 4.2.4), were Λ^0 , Σ^0 and Σ^- . The cross section in terms of the five-fold differential cross section can be expressed as $\frac{d^5\sigma}{dE'd\Omega'_e d\Omega_K^*}$. The electro-production cross section can

then be written in terms of the scattered electron energy E' , electron lab frame solid angle $d\Omega'_e = d \sin \theta_e d\phi_e$, and kaon C.M. solid angle $d\Omega_K^* = d \sin \theta_{qK}^* d\phi$. The model we used is discussed in Section 3.2.3.

CHAPTER 2

EXPERIMENTAL APPRATUS

The experiment was performed at the Thomas Jefferson National Accelerator Facility (Jefferson Lab) in Newport News, Virginia. The electron accelerator is known as the Continuous Electron Beam Accelerator Facility (CEBAF) and is capable of probing nucleon and quark structure in nuclei.

2.1 TJNAF Overview

An aerial view of Jefferson Lab is shown in Figure 2.1. Currently there are three halls using the continuous electron beam from the accelerator. The three halls (namely Hall-A, Hall-B and Hall-C) are shown in Figure 2.1 by three RED circles from left to right respectively. In the future, JLab will upgrade its energy from 6 GeV to 12 GeV, and a new hall (Hall-D) will be added, as shown in Figure 2.2.

2.2 Accelerator

The length of the accelerator is about $7/8$ of a mile for one complete cycle. A polarized electron source at the injector is used to extract electron beam of energy 45 MeV with the standard setup of JLab. The electron beam is accelerated by two linear accelerators, north and south linacs. A series of magnets bends the beam along the arcs which connects



Figure 2.1 Aerial view of Jefferson Lab [18].

the two linacs. The beam line, transporting the beam to the three halls is shown in Figure 2.2 by the RED lines. The continuous-wave (100% duty factor) electron beam from the CEBAF accelerator has a characteristic 2 ns micro-structure that arises from the 1.5 GHz radio frequency (RF) structure of the accelerator and the 499 MHz three-hall beam splitting scheme.

2.2.1 Polarized Source

The production and acceleration of the electron beam starts with a polarized electron source. Circularly polarized light produces polarized electrons from a strained superlattice gallium arsenide (GaAs) cathode through photoemission. This cathode is made up of several layers of material containing GaAs with varying amounts of phosphorus doping, grown on a substrate.

2.2.2 LINAC

Electrons from the injector are sent to the north linear accelerator (linac) at an energy of 45 MeV. Superconducting niobium RF resonant cavities in the north linac section accelerate the electrons; in a standard tune, the maximum gain in energy per linac is 600 MeV in energy. The beam then goes through the east arc and into the south linac to be accelerated for another 600 MeV energy gain. This beam can be sent directly to the Beam Switch Yard (BSY) for distribution to the experimental halls or the beam can be steered along the west arc for another pass through the two linacs for another 1.2 GeV of energy gain. This process can be repeated up to four times. A maximum of five passes through both linacs

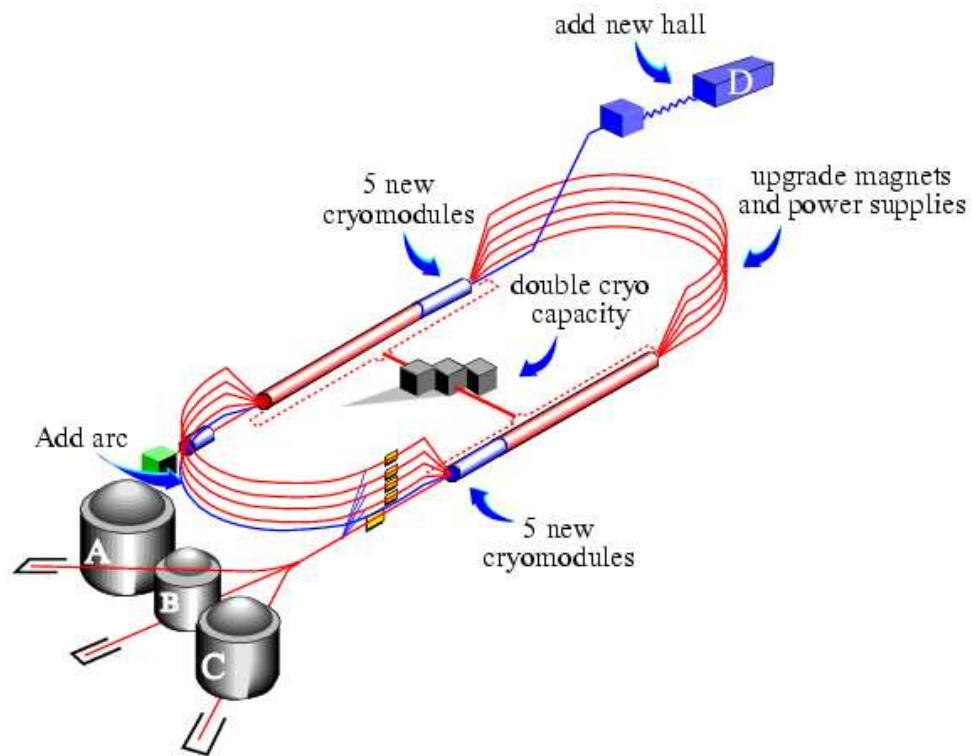


Figure 2.2 Schematic of Jefferson Lab.

Beam is accelerated by two linear accelerator namely north linac and south linac. Three existing Halls A, B, C and one under construction, Hall-D, are shown. The new components that would be added for 12 GeV energy upgrade are also shown in the picture.

provide energies from 445 MeV to 5945 MeV. As the beam energies are different in each pass, a different set of magnets are used to steer the beam around the arcs after each pass.

2.3 Beamline

The beamlines that transport the beam from the accelerator to the experimental halls is shown in Figure 2.2. Each beamline consists of a series of quadrupole and dipole magnets to help focus/ defocus the beam along the way to the target in each hall.

2.3.1 Hall-C Beamline

The beam position, profile and current were measured at various points along the Hall-C beamline. A part of Hall-C beamline also forms an arc. The bending magnets of the Hall-C arc can be used to measure the relative beam energy with a precision of $\Delta E/E \approx 10^{-4}$.

2.3.2 Beam Position Monitor

The beam position was continuously monitored by beam position monitors (BPM) during data collection to ensure that the beam was centered on the target. The transverse beam size was 60-130 μm in diameter and was measured by a superharp (pair of wires that can be moved in and out of the beam) scanner. The BPMs and superharps could measure the beam position with a precision of 0.2 mm and 0.01 mm , respectively [3].

2.3.3 Beam Current Monitor

The beam current was monitored through a combination of a parametric DC current transformer (Unser monitor) and coupled cylindrical resonant cavities(Beam Current Monitor 1 and 2) which provided a continuous relative measurement of the current during each data run [3, 29].

2.3.4 Raster

For liquid targets, the beam was rastered over an area of the target of up to $2 \times 2 \text{ mm}^2$ by the Fast Raster to reach acceptable beam currents without damaging the target and to reduce the effect of localized boiling in the liquid targets.

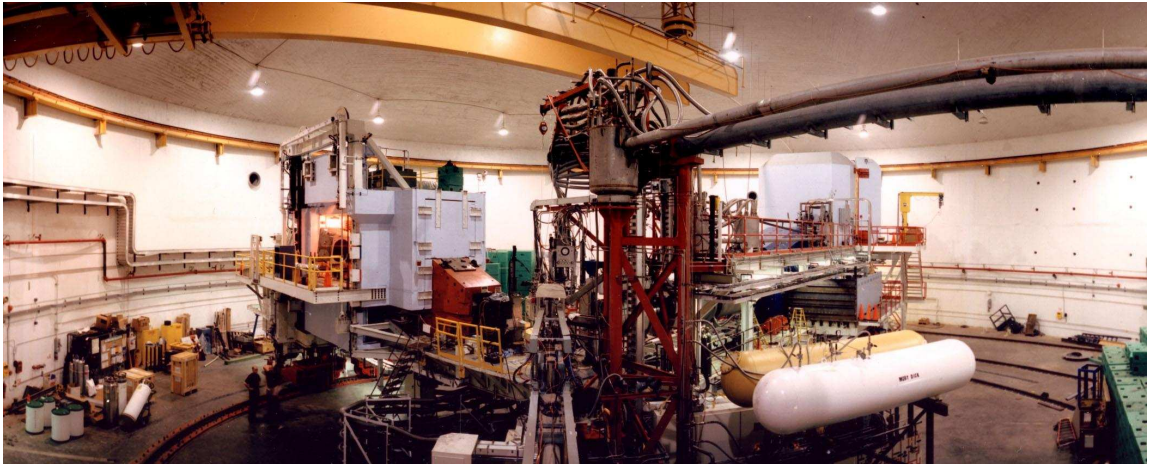


Figure 2.3 Hall C at Jefferson Lab.

2.4 Hall-C

The E01-107 experiment was performed in the Hall-C. Hall-C is shown in Figure 2.3. One can see the beamline is going to the target. There is a Short Orbit Spectrometer (SOS) on the left to collect scattered electrons and a High Momentum Spectrometer (HMS) to collect hadrons on the right at the far end. The unscattered beam is dumped in the Beam Dump at the other end of the hall.

2.4.1 Short Orbit Spectrometer (SOS)

The Short Orbit Spectrometer uses three room temperature magnetic elements: a quadrupole followed by two dipoles (QDD) as shown in Figure 2.4 [11]. The SOS can be rotated about the target in order to detect scattered particles at different scattering angles. In this experiment, scattered electron were detected in the SOS. The configuration of the detectors in the SOS is discussed in Section 2.4.4.

2.4.2 High Momentum Spectrometer (HMS)

The High Momentum Spectrometer is composed of four superconducting magnetic elements in order to focus and separate different particles based on their momentum and charge. In our experiment, π^+ , K^+ and protons were detected in the HMS. The magnetic elements consisted of three quadrupoles followed by a dipole (QQQD) is shown in Figure 2.5 [11]. The HMS can be rotated about the target as well. The configuration of the detectors in the HMS is discussed in Section 2.4.4.

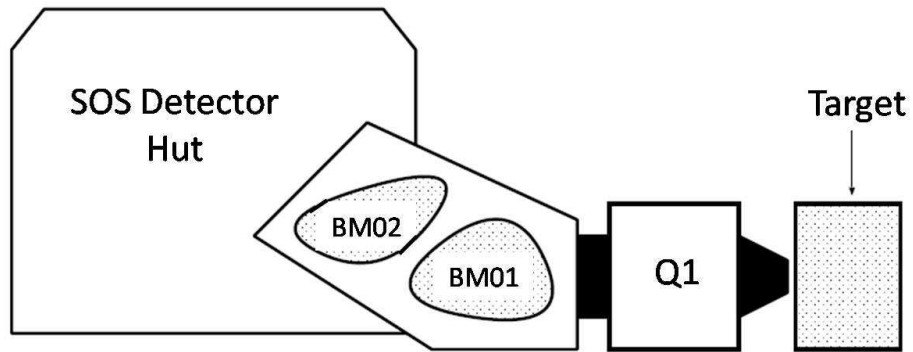


Figure 2.4 Side view of SOS [11].

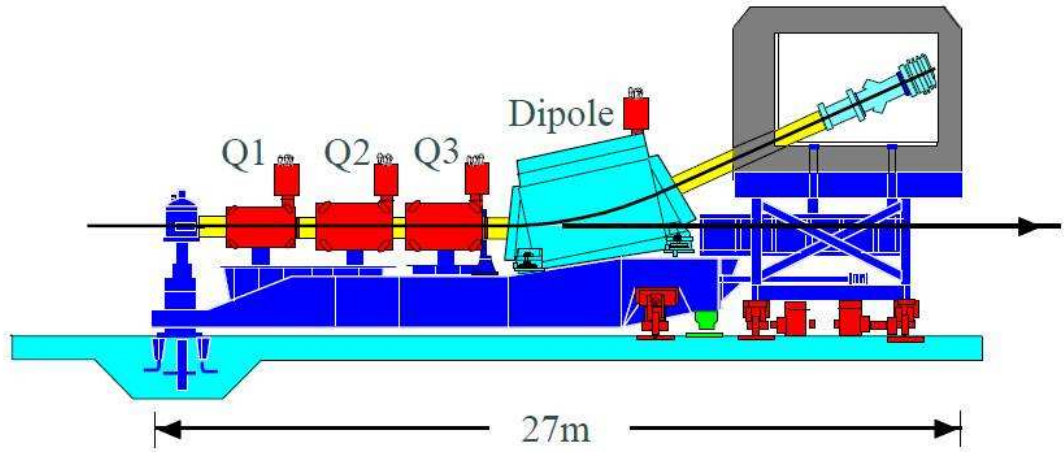


Figure 2.5 Side view of HMS [11].

2.4.3 Target

The electron beam with energy of up to 5.8 GeV was incident on liquid hydrogen and deuterium, and solid foil targets of ^{12}C , ^{27}Al , ^{63}Cu , and ^{197}Au . For the cryotargets, a 4.0 cm diameter cylindrical cell with an axis perpendicular to the beam direction was used. The cell walls with a thickness of 0.01 cm were made from an aluminum alloy. A schematic diagram of the cryogenic target ladder are shown in Figure 2.6. The target ladder could be translated vertically by lifter motors.

2.4.4 Detector Packages

There are two wire chambers each in the HMS and SOS, separated by 81.5 cm in the HMS and by 49.5 cm in the SOS to determine the position and angle of a track. Each wire chamber has six planes of wires and a 1:1 gas mixture of argon and ethane are surrounding

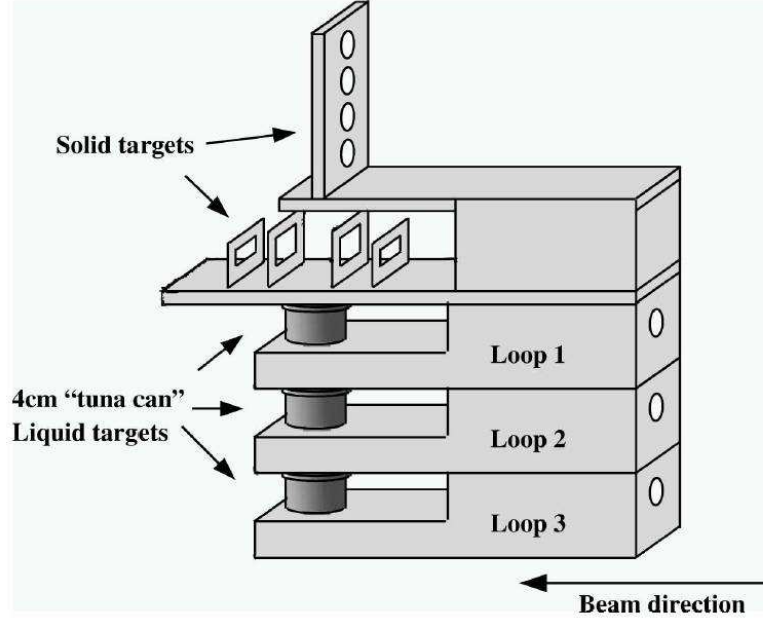


Figure 2.6 Schematic diagram of target ladder [3].

the wires. The position resolutions of the HMS and SOS drift chambers were $280 \mu\text{m}$ and $180 \mu\text{m}$, respectively [3, 34].

Four planes of scintillator hodoscopes are used both in the HMS and in the SOS to form the primary trigger for charged particle detection. These four planes were used to identify a particle that passed through them and produced signals.

Čerenkov detectors were used to detect the Čerenkov radiation emitted when a particle enters a medium and moves faster than the speed of light in that medium. Two types of Čerenkov detectors were used for particle identification (PID): Aerogel Čerenkov and Gas Čerenkov. Silica aerogel Čerenkov of refractive index $n = 1.015$ with threshold for π^+ of $0.8 \text{ GeV}/c$ and a threshold for K^+ of $2.85 \text{ GeV}/c$ was used; this allowed us to separate particles traveling above and below the threshold. A gas Čerenkov detector filled with 0.956 atm of perfluorobutane (C_4F_{10}) with an index of refraction of 1.0015 and a

momentum threshold of 2.65 GeV/c for π^+ and threshold of 9.4 GeV/c for K^+ was used for PID as well [3].

2.5 Data Acquisition

The CEBAF Online Data Acquisition (CODA) software system managed real time reading of the data, its storage to disk as well as user interface [1]. Read Out Controller (ROC) CPUs managed the readout electronics, ADCs, TDCs and scalers. CODA software also read the ROCs directly via a parallel link over an ethernet network and wrote each event onto disk. Information about the beam position, magnet settings, target status and accelerator status were read out every 30 seconds using Experimental Physics Industrial Control System (EPICS) software [29].

2.6 Kinematic Settings

The E01-107 experiment was carried out in Hall C at Jefferson Lab [22] in 2004. The kinematic settings of the measurements are shown in Table 2.1. The experiment was designed to measure the nuclear transparency of pions using the $(e, e'\pi^+)$ reaction for five kinematic settings of $Q^2 = 1.1, 2.15, 3.0, 3.91$ and 4.69 (GeV/c)². In addition to pions a reasonable sample of kaons were also recorded in the 30 ns coincidence window. The kaon statistics were very low for $Q^2 = 3.91$ and 4.69 (GeV/c)² kinematic settings, hence this analysis covers only three kinematic settings, as listed in Table 2.1.

More details of the experimental apparatus can be found in references [3, 29, 34].

Table 2.1 The central kinematics of the experiment.

Q^2 (GeV/c) ²	$-t$ (GeV/c) ²	E_e GeV	$\theta_{e'}^{\text{SOS}}$ deg	$E_{e'}$ GeV	θ_{K^+} deg	θ_{HMS} deg	p_{K^+} GeV/c
1.10	0.050	4.021	27.76	1.190	10.58	10.61	2.793
2.15	0.158	5.012	28.85	1.730	13.44	13.44	3.187
3.00	0.289	5.012	37.77	1.430	12.74	12.74	3.418

CHAPTER 3

MONTE CARLO SIMULATION

3.1 General Overview

In order to take into account the multi-dimensional phase space of the experiment, this analysis required a Monte Carlo simulation of the experiment to extract the yield of K^+ s which is used to extract the nuclear transparency. The simulation uses a model of the electro-production of kaons from protons which includes multiple scattering, energy loss from passage through materials, kaon decay, and correction due to radiative processes.

The simulation code used for this analysis was based upon the code SIMULATE used by the SLAC NE-18 experiment [14]. The code has been modified to include magnetic transport models of the spectrometer, HMS and SOS of Hall-C in Jefferson Lab and has been renamed as SIMC.

3.2 Ingredients of SIMC

In this section we give an overview of some of the basic ingredients of SIMC.

3.2.1 Event Generation

The event generator for electron-proton scattering consists of randomly generated energy-momentum 4-vectors for all the initial and final particles within the constraints of

energy-momentum conservation in a two-body reaction (the kaon-hyperon production is a two-body process). The incident electron 4-vector is generated from the known beam energy, randomly smeared by the energy resolution (0.1%). The target proton 4-vector just requires the proton mass since it is at rest. The outgoing particles 4-vectors are generated within the allowed acceptance of the spectrometers. The event generation also randomly picks an interaction point that is within the length of the target and consistent with the beam raster amplitude used in the experiment. With this complete set of information on the interaction vertex, we can calculate the physics variables Q^2 , W , t and ϕ_{pq} . Here Q^2 is four-momentum transferred square, W is the C.M. energy, t is the momentum transfer and ϕ_{pq} is the angle between the scattering and reaction planes. The event generation is performed for the selected species of hyperons $Y = (\Lambda^0, \Sigma^0, \Sigma^-)$.

3.2.2 Spectrometer Simulation

SIMC has realistic models of the magnetic spectrometers including multiple scattering and energy loss in all intervening material encountered by the particles. All outgoing particles are transported through the magnets to the detector huts by a set of matrix elements that model the passage of charged particles through the magnetic elements of the spectrometer. The position and angle (track) information, smeared by the wire-chamber resolution, at the focal plane of the spectrometer are calculated for all particles that make it through the detector elements. The smeared track at the focal plane is then reconstructed back to the target using another set of matrix elements. This mimics the method used to analyze the data.

3.2.3 Physics Model

The kaon electro-production from a proton is depicted in Figure 3.1. A model of this reaction is in the simulation, SIMC. The five fold-differential cross section for this process can be expressed in terms of a photoproduction cross section $\frac{d^2\sigma}{d\Omega_K^*}$ multiplied by a virtual photon flux factor $\Gamma(Q^2, W)$.

$$\frac{d^5\sigma}{dQ^2 dW d\phi_e d\Omega_K^*} = \Gamma(Q^2, W) \left(\frac{d^2\sigma}{d\Omega_K^*} \right) \quad (3.1)$$

In the simulation, a transformation between $(Q^2, W) \leftrightarrow (E', \Omega'_e)$ is incorporated into the virtual photon flux, where E' is energy of the scattered electron and Ω'_e is electron lab frame solid angle, using

$$\Gamma(Q^2, W) = \Gamma_0(E', \Omega'_e) \frac{W}{2m_p E E'} = \frac{\alpha}{4\pi^2} \frac{(W^2 - m_p^2)}{2m_p^2 E^2} \frac{W}{Q^2} \frac{1}{(1 - \epsilon)} \quad (3.2)$$

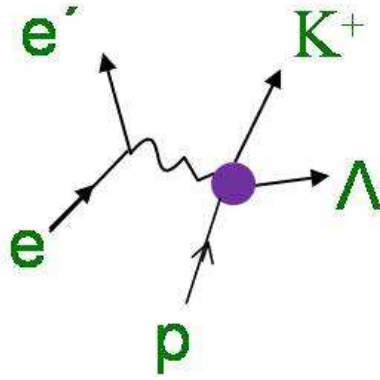


Figure 3.1 Schematic of kaon electro-production from a proton.

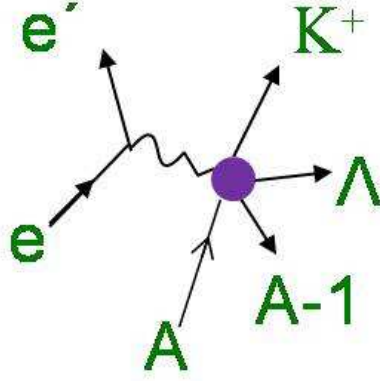


Figure 3.2 Schematic of kaon electro-production from different targets.

where m_p is the mass of the proton and $\epsilon = \left(1 + \frac{2|\vec{q}|^2}{Q^2} \tan^2 \frac{\theta_e}{2}\right)$ is the longitudinal polarization of the virtual photon.

The model for electro-production from nuclear targets schematically shown in Figure 3.2 was built from a parameterization of the measured cross section from a hydrogen target; for all other heavier targets (carbon, copper, gold) proton model is convoluted with a realistic spectral function for each target parametrized in terms of Eqs. 3.1 and 3.2. Decay of kaons in flight and radiative corrections for all particles are also included in the model.

3.2.4 Kaon Decay

In general, kaons are unstable and have a short mean lifetime which implies that a large fraction of the kaons which were created at the target decayed into secondary particles before they could be detected. The number of kaons that were actually detected was less than the true number of kaons produced in the reaction and corrections for their decay has been taken into account in the analysis [29]. Kaon decay, multiple scattering, and energy

loss are standard features in SIMC, and can be turned on and off using flags in the input files. Descriptions of corrections for these processes in the SIMC can be found in [11].

3.2.5 Spectral Function

The quasi-free model is used to describe electro-production from different nuclear targets used in the experiment. The incoming electron has larger energy compared to the binding energy of nucleons in the nucleus. So the bound nucleons in the target nucleus may be viewed as free nucleons. Properties of the nucleons inside of the nucleus are assumed to be described by an independent particle shell model, where each nucleon interacts with a mean field exerted by the other nucleons [3]. The probability of finding a nucleon inside the nucleus with a certain energy and momentum can be defined by a spectral function. For heavier targets, the proton model is convoluted with a realistic spectral function for each target.

3.3 Comparison of Data with SIMC

One of the goal of this analysis is to determine the normalized yields from the raw data collected during the experiment. The normalized yield is the number of events that pass a given set of cuts divided by the cumulative charge delivered by the beam and corrected for the various inefficiencies of the experimental equipment.

Before calculating the yields, we compare the data with SIMC yields, to verify that the Monte Carlo distributions agree with the measured distributions for these variables. If the shape of these distributions agree, it validates our model of kaon electro-production.

The target quantities (horizontal slope X'_{tar} , vertical slope Y'_{tar} and the momentum fraction of the particle with respect to the spectrometer central momentum δ) were reconstructed using the focal plane quantities X_{fp} (horizontal position), X'_{fp} (horizontal angle), Y_{fp} (vertical position) and Y'_{fp} (vertical position) on the focal plane¹ for HMS and SOS. The reconstructed angle and momentum fraction at the target are labeled as *hsxptar*, *hsyptar* and *hsdelta* for the HMS and *ssxptar*, *ssyptar* and *ssdelta* for the SOS.

Beside applying cuts on Q^2 , W , t and ϕ_{pq} , cuts were applied on these reconstructed quantities (such as *hsxptar*, *ssxptar*, *hsyptar*, *ssyptar*, *hsdelta* and *ssdelta*) both on the data and SIMC yields, as they define the fiducial acceptance of the detector. In order to restrict the data to regions where they match the simulation, we applied very tight cuts on these fiducial acceptances. The cuts are discussed in Section 4.3.

As a representative sample, we have shown the comparison of data with SIMC yields for the reconstructed target variables in the case of Λ production at $Q^2 = 2.2$ (GeV/c)². BLUE and RED show data and SIMC, respectively, for the HMS in Figure 3.3 and for the SOS in Figure 3.4. Similarly comparisons were also performed for Λ and Σ production at $Q^2 = 1.1$ to 3.0 (GeV/c)², but are not shown here.

¹Focal plane is perpendicular to the central ray.

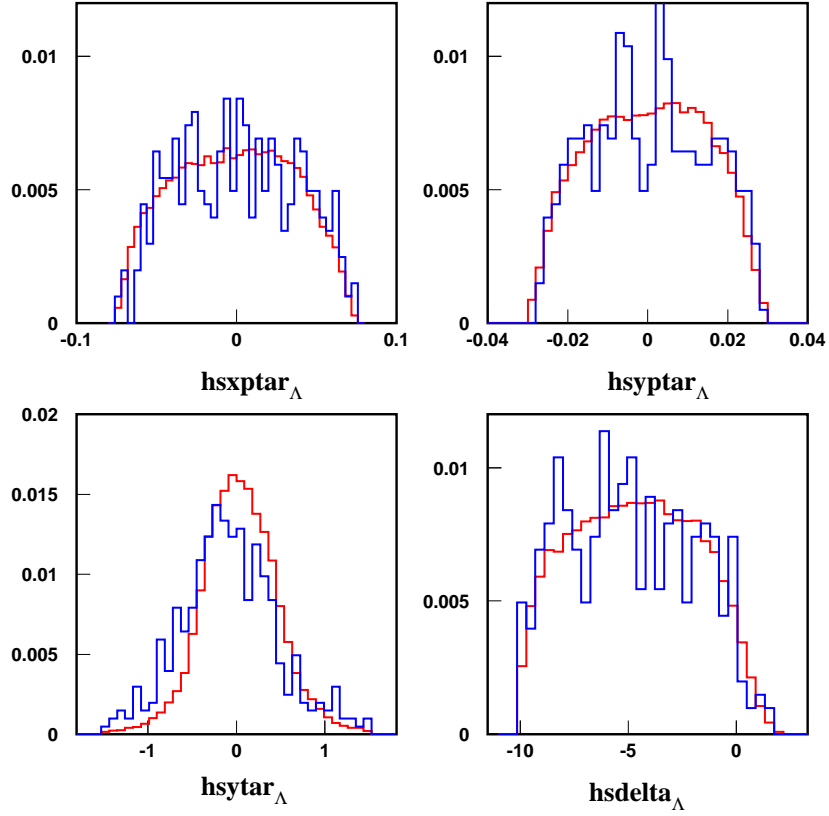


Figure 3.3 HMS reconstructed angles and momentum fraction.

$hsxptar$, $hsyptar$, $hsytar$ and $hsdelta$ for Λ production of K^+ after applying cuts on the variables. RED for SIMC and BLUE for data.

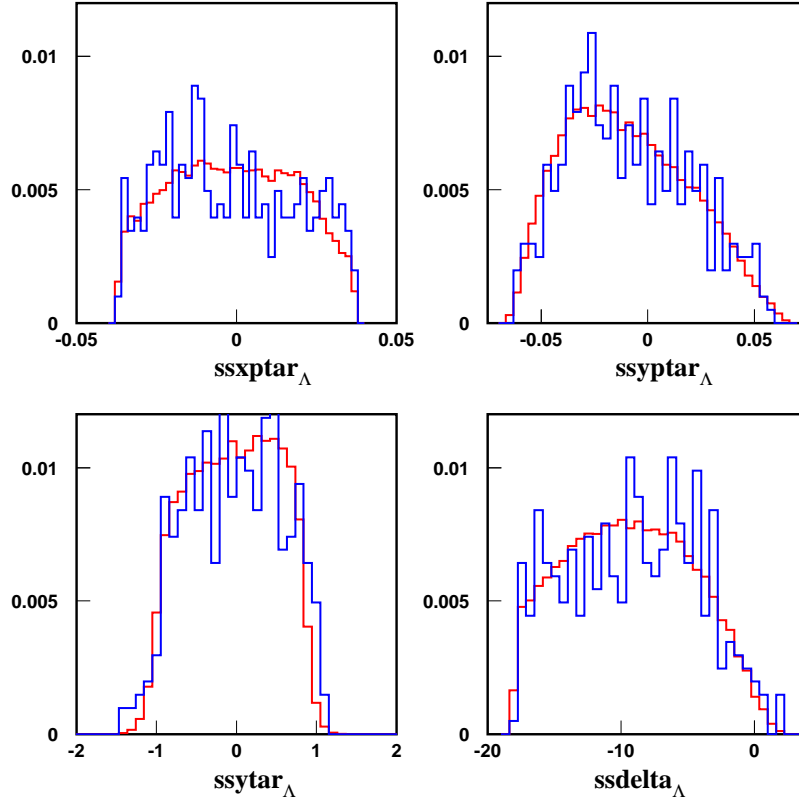


Figure 3.4 SOS reconstructed angles and momentum fraction.

$ssxptar$, $ssyptar$, $ssytar$ and $ssdelta$ for Λ production of K^+ after applying cuts on the variables. RED for SIMC and BLUE for data.

CHAPTER 4

ANALYSIS

4.1 General Overview

One of the goals of the analysis is to determine the normalized yields from the raw data collected during the experiment. The normalized yield is the number of events that pass a given set of cuts divided by the cumulative charge delivered by the beam and corrected for various inefficiencies of the experimental equipment. We have extracted nuclear transparency by forming a super ratio of the experimental yield to the Monte Carlo simulation yield from given targets with nucleon number A and deuterium. This ratio is shown in the expression below:

$$T = \left(\frac{\bar{Y}}{\bar{Y}_{MC}} \right)_A / \left(\frac{\bar{Y}}{\bar{Y}_{MC}} \right)_D, \quad (4.1)$$

\bar{Y} is experimental charge-normalized data yield and \bar{Y}_{MC} is the charge-normalized Monte Carlo equivalent yield. In this chapter, we will describe the steps involved in extracting the normalized yields and transparency. For determining the nuclear transparency of kaons, we have reconstructed the physical variables Q^2 , W , t and ϕ_{pq} for each event at the interaction vertex. The measured yield is an integral over all of these variables.

4.2 Particle Identification(PID)

We have used particle track information from drift chambers, time-of-flight information from scintillators, response from a gas Čerenkov detector and an aerogel Čerenkov detector to identify the kaons and separate them from other hadrons, such as pions and protons.

4.2.1 Tracking

The drift chambers provide the position, angle and momentum (relative to the central momentum) of the particles passing through the spectrometer. We have applied cuts on the reconstructed position, angle and momentum to ensure that they are well within the spectrometer acceptance. Due to poor statistics at the edges of the acceptance, tight cuts were applied on these variables to ensure a good match between the data and SIMC yields.

4.2.2 Charge-Normalized Yield

The charge normalized yield can be defined as

$$\bar{Y} = \frac{Y}{Q} \quad (4.2)$$

where Y is the yield of a given run in counts and Q is the charge delivered by beam (in mC), measured by Beam Current Monitors (BCM) and integrated over the time duration of a run. The yield is given by

$$Y = \frac{N_{true}}{[\epsilon_{scer}\epsilon_{track}f_{elec}]_{SOS}[\epsilon_{hcer}\epsilon_{haero}\epsilon_{track}/f_{elec}]_{HMS}} \frac{N_{pretrigger}}{N_{trigger}} \frac{1}{T_h} \quad (4.3)$$

where N_{true} is the true number of events, f_{elec} is electronic dead-time correction factor, ϵ_{hcre} is the HMS Čerenkov efficiency, ϵ_{scer} is the SOS Čerenkov efficiency, ϵ_{aero} is the HMS aerogel efficiency, ϵ_{track} is the HMS/SOS tracking efficiency and $\frac{N_{trigger}}{N_{pretrigger}}$ is the lifetime. The transmission through the target material, the window of the scattering chamber, the windows of the spectrometer, etc. are collectively referred to as T_h .

4.2.3 Coincidence Time

Coincidence time is defined as the difference of the time taken by the scattered electrons to reach the SOS to the time taken by the hadrons (p , π^+ , K^+) to reach the HMS. Good coincidence timing is the most useful and important information used to achieve clean real K^+ yield and helps to measure the insufficiencies of the most of the other cuts.

The time-of-flights (TOF) of the electron in the SOS and of hadrons in the HMS were obtained from the TOF scintillator detectors in each spectrometer. These were used to determine the coincidence time, which is the relative time difference between the electron and the hadron projected back to the target. Cuts on coincidence time were used to separate kaons from pions and protons.

A typical plot of the coincidence time of the experiment is shown in Figure 4.1. Since the experiment was designed for pions, one can see a sharp peak of π^+ in the 30 ns coincidence window. There is a broad peak of protons as well and between protons and π^+ peak there is a rather small peak of kaons. In Figure 4.1, the small periodic peaks at an

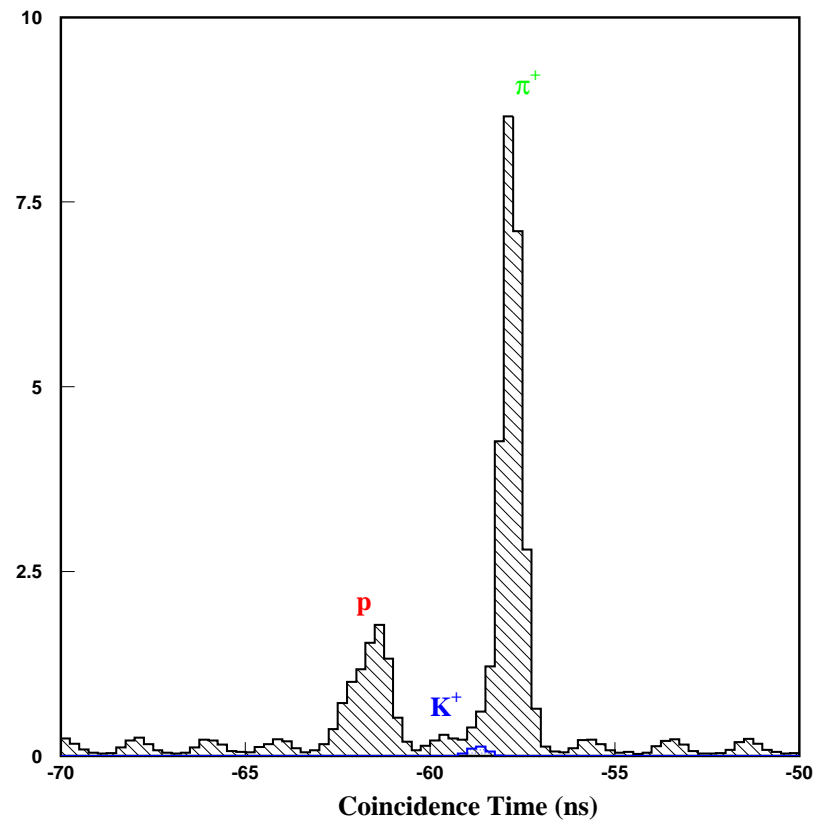


Figure 4.1 Coincidence time plot of the experiment.

The broad peak in the right side is from π^+ , proton peak in the left and reasonable number of K^+ in the middle shown in BLUE.

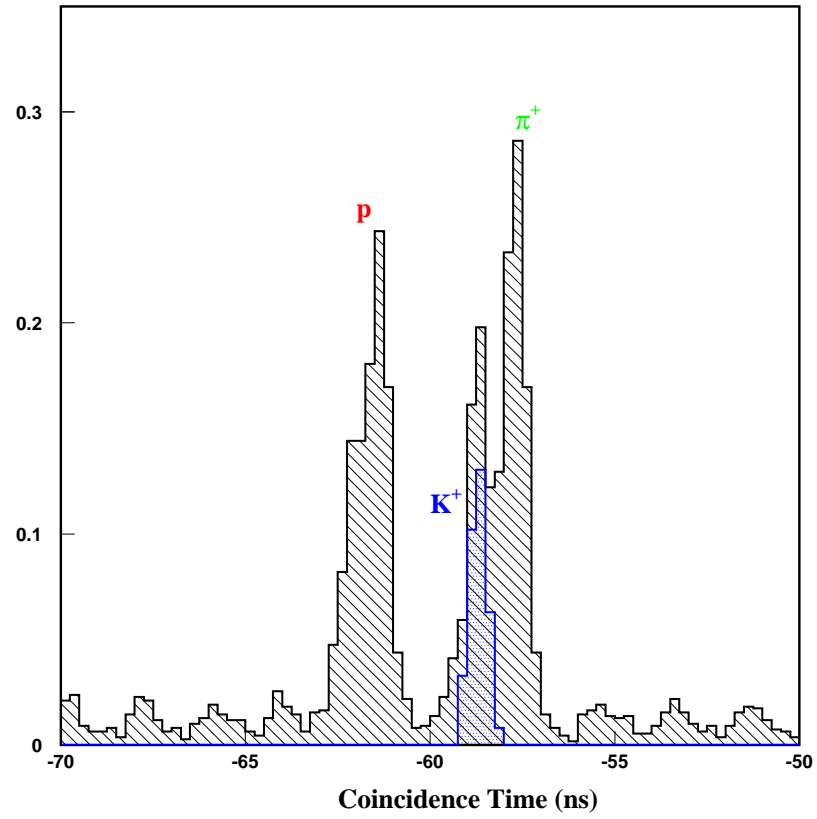


Figure 4.2 Zoomed coincidence time plot of the experiment.

The selected peak of K^+ in BLUE in the middle from π^+ and proton peak in the right and left, respectively, after applying all the cuts.

interval of 2.004 ns are due to the 499 MHz pulse structure of the beam delivered by the accelerator to Hall-C. One of the most effective PID cuts was over coincidence time in order to separate K^+ from π^+ and protons. Selected kaons after applying all the cuts are shown by BLUE region in Figure 4.2.

The fraction of electron-kaon coincidences that were uncorrelated accidental coincidences must be corrected in order to arrive at the true electro-production yield. The accidental coincidences have been corrected using the average number of kaon events in three of the small peaks that are 2.004 ns apart on both sides of the central coincidence time peak and has been shown by the GREEN band in Figure 4.5.

4.2.4 Missing Mass

To understand missing mass, we need to look into the basic reactions of the experiment, which can be written as

$$e + p \rightarrow e' + K^+ + \Lambda^0 \quad (4.4)$$

$$e + p \rightarrow e' + K^+ + \Sigma^0 \quad (4.5)$$

$$e + n \rightarrow e' + K^+ + \Sigma^- \quad (4.6)$$

In the nucleus, the reaction can be written as

$$e + A \rightarrow e' + K^+ + \Lambda^0 + X \quad (4.7)$$

$$e + A \rightarrow e' + K^+ + \Sigma^0 + X \quad (4.8)$$

$$e + A \rightarrow e' + K^+ + \Sigma^- + X \quad (4.9)$$

Since the Λ/Σ are not detected, from energy and momentum conservation we can write from Eq. 4.4, 4.5 and 4.6,

Energy conservation:

$$E_e + M_p = E_{e'} + E_{K^+} + E_X \text{ or, } E_X = E_e + M_p - E_{e'} - E_{K^+} \quad (4.10)$$

Momentum conservation:

$$P_e + 0 = P_{e'} + P_{K^+} + P_X \text{ or, } P_X = P_e + 0 - P_{e'} - P_{K^+} \quad (4.11)$$

Then we can form a variable called missing mass as

$$M_X = \sqrt{E_X^2 - P_X^2} \quad (4.12)$$

Those events which have a missing mass equal to the Λ^0 particle can be identified as being produced in the $e + p \rightarrow e' + K^+ + \Lambda^0$ reaction. By placing a cut on M_X around M_{Λ^0} , we can choose those K^+ produced in the first reaction shown above. Similarly, by cutting on the missing mass around the Σ^0 and Σ^- mass, we can select the K^+ produced from the second and third reactions, respectively.

The basic idea is to use the reconstructed missing mass and cuts around the various hyperons masses to separate K^+ from p and π^+ as well as to separate the Λ from Σ^0 and

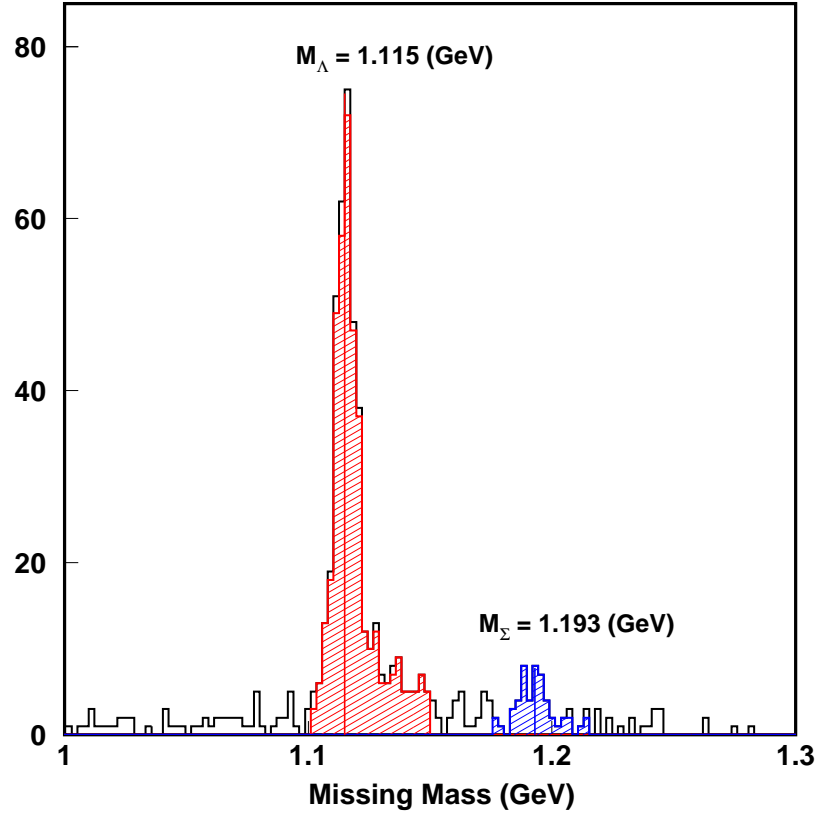


Figure 4.3 One-dimensional missing mass plot.

First sharp peak is due to Λ production and second small peak is due to Σ production of kaons.

Σ^- production of K^+ from protons. As the statistics were very low, it was very difficult to separate Σ^0 and Σ^- for the events. We did not try to distinguish between the production of Σ^0 and Σ^- . More details follow in Section 5.1.

Using the missing mass variable for hydrogen data, we have separated K^+ from Λ and Σ production. From these events, we determine a ratio of $\frac{\Lambda}{\Sigma}$. We used this same ratio in the Monte Carlo simulation. In targets heavier than hydrogen, the Fermi motion¹ of the

¹The quantum motion of nucleons bound inside a nucleus is known as Fermi motion.

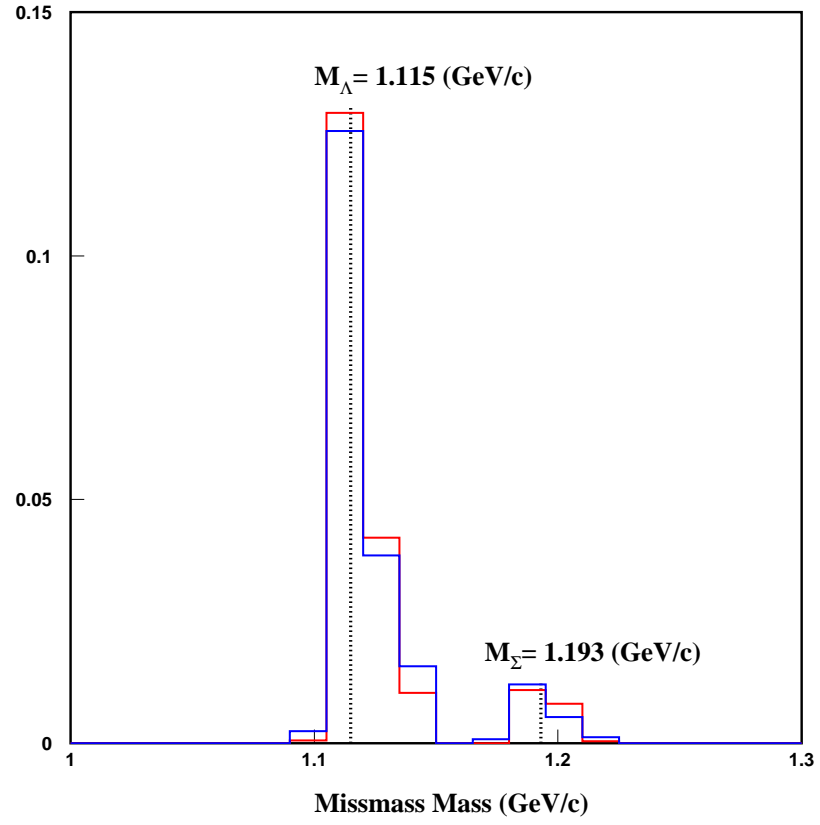


Figure 4.4 One-dimensional missing mass plot after applying cuts.

M_{Λ}^{SIMC} and M_{Σ}^{SIMC} are shown in RED and M_{Σ}^{data} and M_{Λ}^{data} are in BLUE.

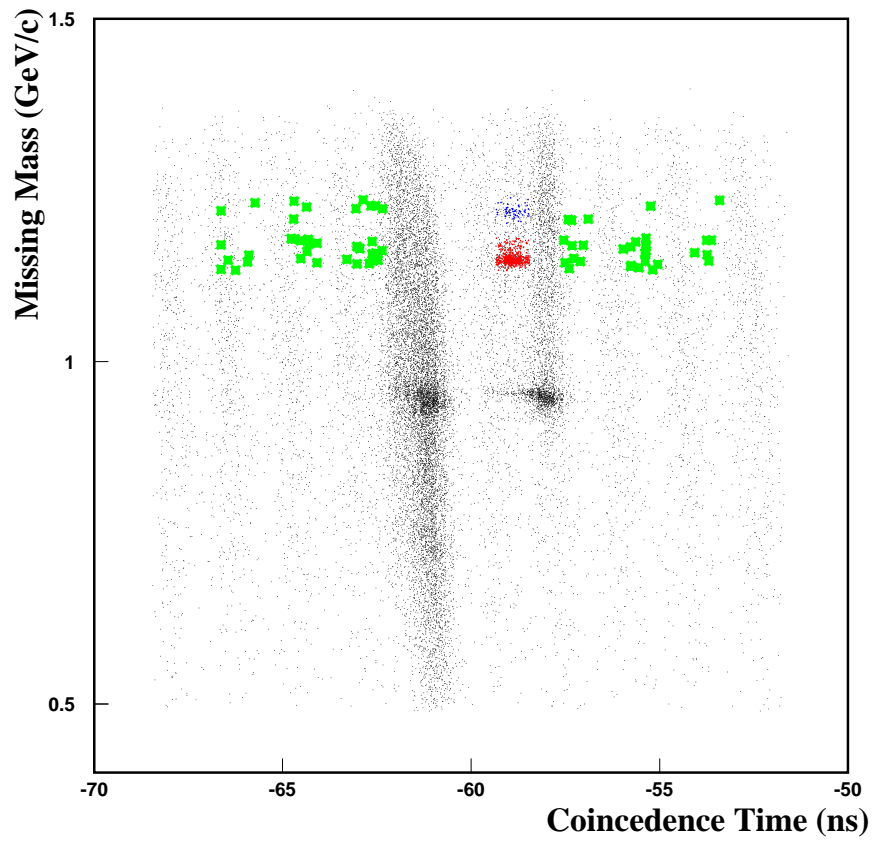


Figure 4.5 Two-dimensional plot of missing mass vs coincidence time.

p , K^+ and π^+ are shown here from left to right, respectively, after applying loose cuts.

nucleons begin to broaden the Λ and Σ peak and are very difficult to distinguish. For all other targets due to the spreading of Λ and Σ , we used a single cut over both Λ and Σ masses to separate K^+ .

The missing mass spectrum shown in Figure 4.3 is from the hydrogen target for $Q^2 = 1.1 \text{ (GeV/c)}^2$. In Figure 4.3, the BLACK region represents events without any cut and the RED region represents the application of the cut on missing mass for K^+ production from Λ and BLUE shows from the Σ channel, whereas the RED vertical line at $M_\Lambda = 1.115 \text{ (GeV/c)}^2$ shows the mass of Λ and BLUE vertical line at $M_\Sigma = 1.193 \text{ (GeV/c)}^2$ shows the mass of Σ from [6]. For Σ mass we have taken average of the mass of Σ^0 and Σ^- since we have two Σ channels; given our meagre statistics, we are unable to separate Σ^0 and Σ^- productions.

The missing mass variable is shown in Figure 4.4 after applying all the cuts where the SIMC yields are shown by RED and data by BLUE. Λ and Σ production have been separated by using the hydrogen data. Figure 4.5 shows two-dimensional plot of missing mass vs coincidence time. The Λ events are shown in RED and Σ in BLUE.

4.2.5 Čerenkov Radiation

Two type of Čerenkov detectors, i.e, aerogel and gas Čerenkov, have been used to identify particles in the experiment. The aerogel Čerenkov detector used in the experiment has a refractive index of $n = 1.015$. In Figure 4.6 we show the threshold for producing Čerenkov radiation by proton (RED curve), pions (GREEN curve), and kaons (BLUE curve). From this figure, we see that in our experiment the protons never produce

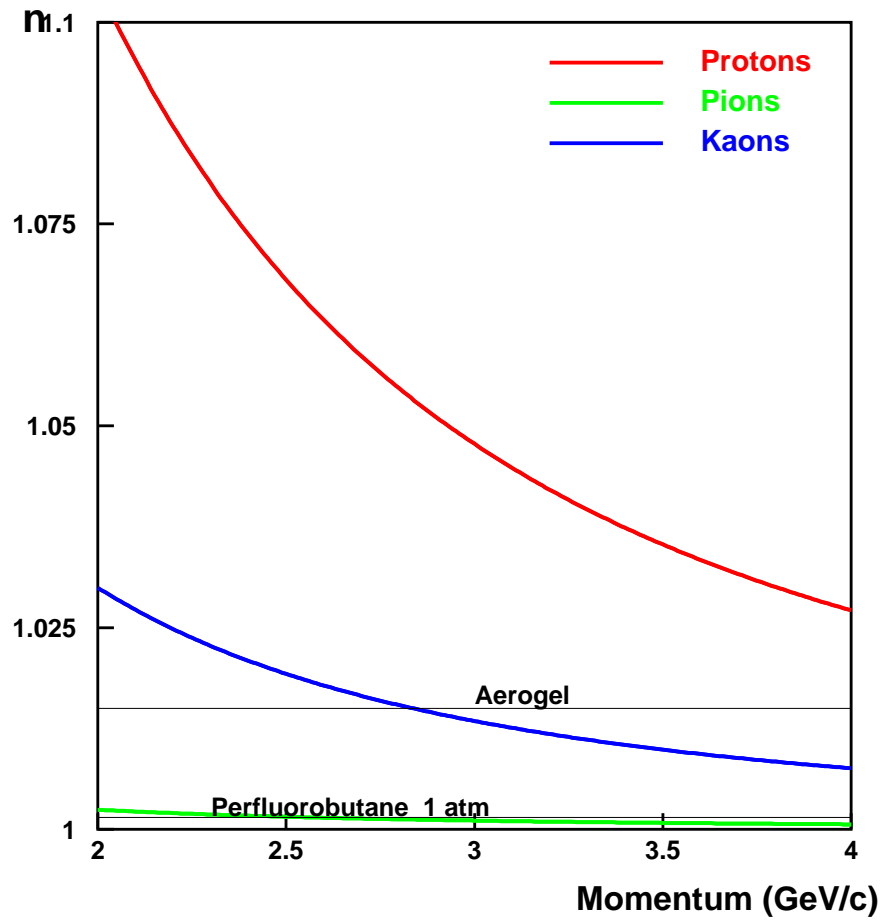


Figure 4.6 Aerogel Čerenkov detector.

Proton, pion and kaon thresholds for producing Čerenkov radiation in the aerogel Čerenkov detector are shown by RED, GREEN and BLUE curves respectively.

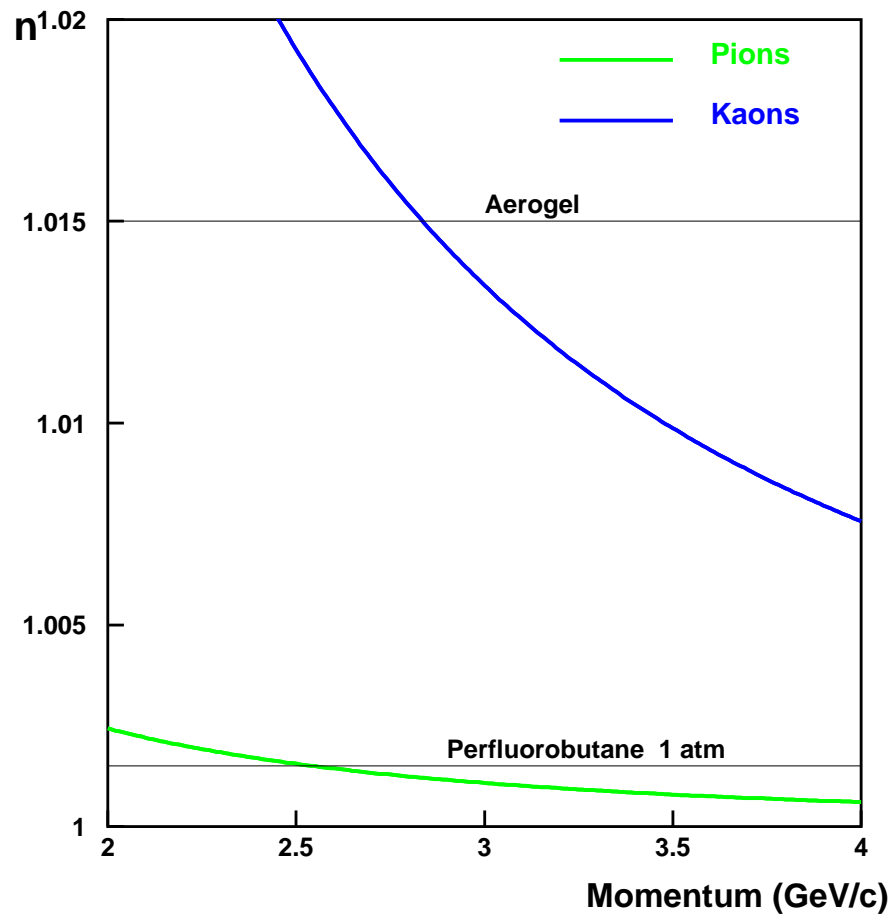


Figure 4.7 Gas Čerenkov detector.

Kaon and pion thresholds for producing Čerenkov radiation in the gas Čerenkov detector are shown by BLUE and GREEN curves, respectively.

Čerenkov radiation in the aerogel detector because the proton momentum in the experiment ($P_p = 2.7 - 3.4 \text{ (GeV/c)}$) is always above the threshold, while the kaons produce Čerenkov radiation for all kinematics except the $Q^2 = 1.1 \text{ (GeV/c)}^2$ kinematics where the kaon momentum is $P_K = 2.7 \text{ (GeV/c)}$ which is above threshold for the aerogel. The pions are always below threshold and produce Čerenkov radiation for all kinematics. By applying cuts on the number of photo-electrons detected in the aerogel detector we could separate the protons from kaons and pions at all kinematics except $Q^2 = 1.1 \text{ (GeV/c)}^2$.

The gas Čerenkov detector uses perfluorobutane at 1 atmosphere which has a refractive index of 1.0015. In Figure 4.6, the thresholds for pion and kaon are being shown by GREEN and BLUE curve, respectively. Kaons could be separated from pions by cutting on gas Čerenkov signal. If we apply cuts on the gas Čerenkov signal, then we will be able to separate kaons from pions. So, applying cuts on the two Čerenkov detectors we could separate kaons from pions and protons.

4.3 Cuts

The cuts applied on the reconstructed variables are shown in Table 4.1. The cuts applied on data and the SIMC yields were the same for all cases. We have applied very tight cuts on all the variables to restrict the data to regions where the shape of that variable matches with SIMC yields.

The cuts applied on data or SIMC yields for kinematics of $Q^2 = 2.2 \text{ (GeV/c)}^2$ have been shown in Table 4.1. Most of the cuts applied on all the variables were quite similar for all the kinematics. We separated Λ and Σ production of K^+ for hydrogen data for all

Table 4.1 Cuts applied on the reconstructed variables for data or SIMC.

Variables	Left	Right
Coincidence Time	-59.21	-58.13
$MissingMass_{\Lambda}$	1.10	1.15
$MissingMass_{\Sigma}$	1.175	1.215
hsxptar	-0.075	0.075
hsyptar	-0.03	0.03
hsdelta	-10	5
ssxptar	-0.065	0.065
ssyptar	-0.0375	0.0375
ssdelta	-18	5
Q^2	1.4	2.5
W	2.18	2.48
t	0.23	0.52
ϕ_{pq}	1.5	5

the variables. As we went to the heavier targets, the regions for Λ and Σ production seems to merge for almost all the variables and hence we were not able to separate them. So, the cuts applied for all other targets were similar with each other except for hydrogen.

4.3.1 Other Cuts

Cuts were applied on several other reconstructed variables, such as *hsxptar*, *hsyptar*, *ssxptar*, *ssyptar*, *hsdelta*, *ssdelta*, etc., which define the fiducial acceptance of the detector. These cuts have been applied to restrict the data to regions where they match the simulation. These cuts were discussed in the previous chapter.

4.4 Comparison of Data with SIMC Yields

The cross section depends upon four variables; they are Q^2 , W , t , ϕ_{pq} , where Q^2 is four- momentum transferred square, W is the C.M. energy, t is momentum transfer, and ϕ_{pq} is the angle between the scattering and reaction planes. So before calculating transparency, we compare the data with SIMC yields for these variables. If the simulated shape of these variables agree with the data, we can claim that the model used in the SIMC simulation is valid. After adding Λ and Σ production for K^+ with proper ratio obtained using hydrogen data, the yields are shown in Figure 4.9 for variable Q^2 . The same procedure was applied to other variables as well. Comparison of data yields and SIMC yields for the variables W , t and ϕ_{pq} after adding Λ and Σ production for K^+ are shown in Figure 4.10, Figure 4.11 and Figure 4.12, respectively.

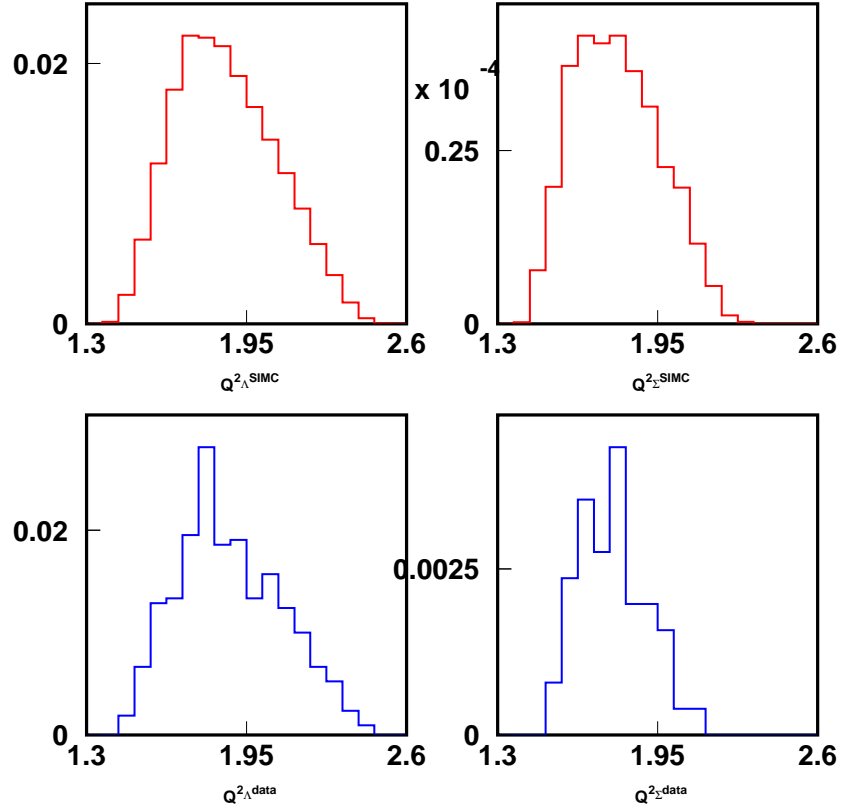


Figure 4.8 Comparison of Q^2 from data and SIMC.

Clockwise from top left corner: $Q^2_{\Lambda} \text{ SIMC}$, $Q^2_{\Sigma} \text{ SIMC}$, $Q^2_{\Sigma} \text{ data}$, $Q^2_{\Lambda} \text{ data}$ for $Q^2=2.2 \text{ (GeV}/c)^2$, where SIMC and data are shown in RED and BLUE, respectively.

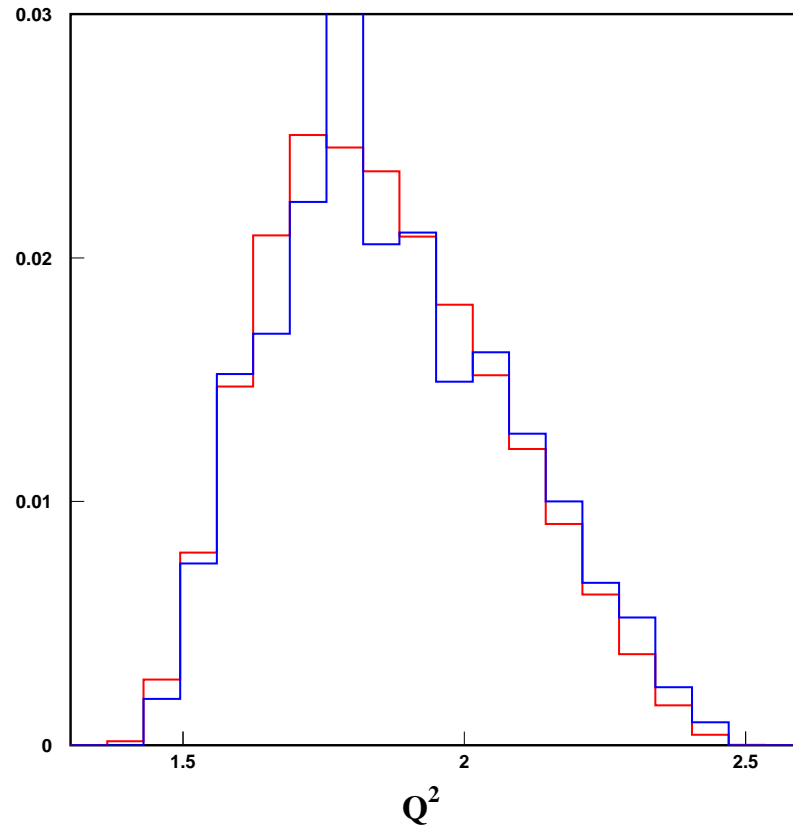


Figure 4.9 Comparison of Q^2 from data and SIMC.

Q^2 combined Λ and Σ for both SIMC and data yields in RED and BLUE respectively for $(\text{GeV}/c)^2$.

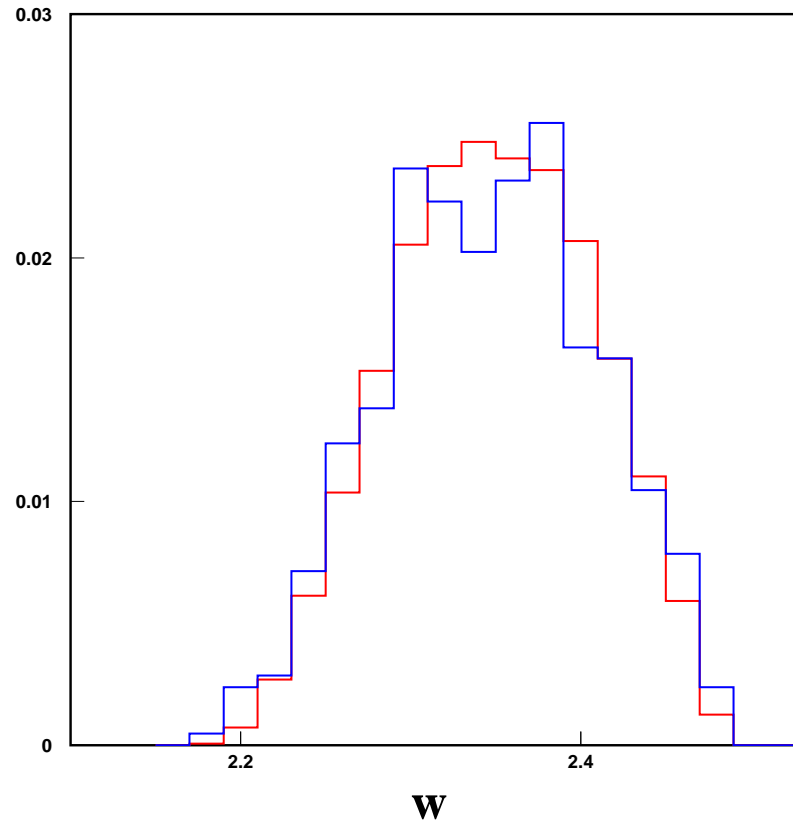


Figure 4.10 Comparison of W from data and SIMC.

W combined Λ and Σ for both SIMC and data yields in RED and BLUE, respectively, for $Q^2=2.2$ (GeV/c)².

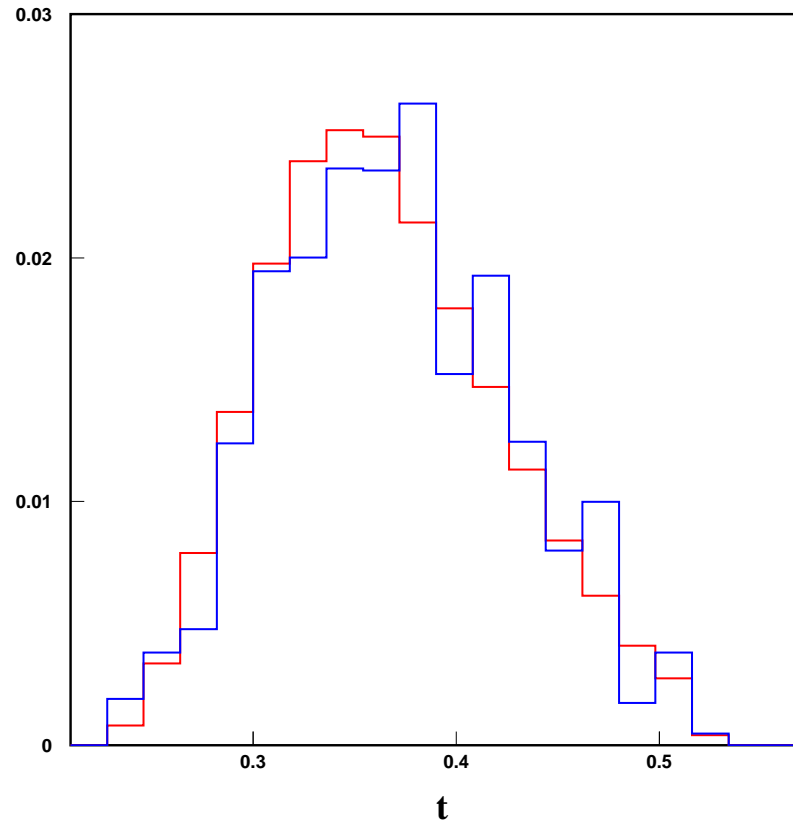


Figure 4.11 Comparison of t from data and SIMC.

t combined Λ and Σ for both SIMC and data yields in RED and BLUE, respectively, for $Q^2=2.2$ (GeV/c) 2 .

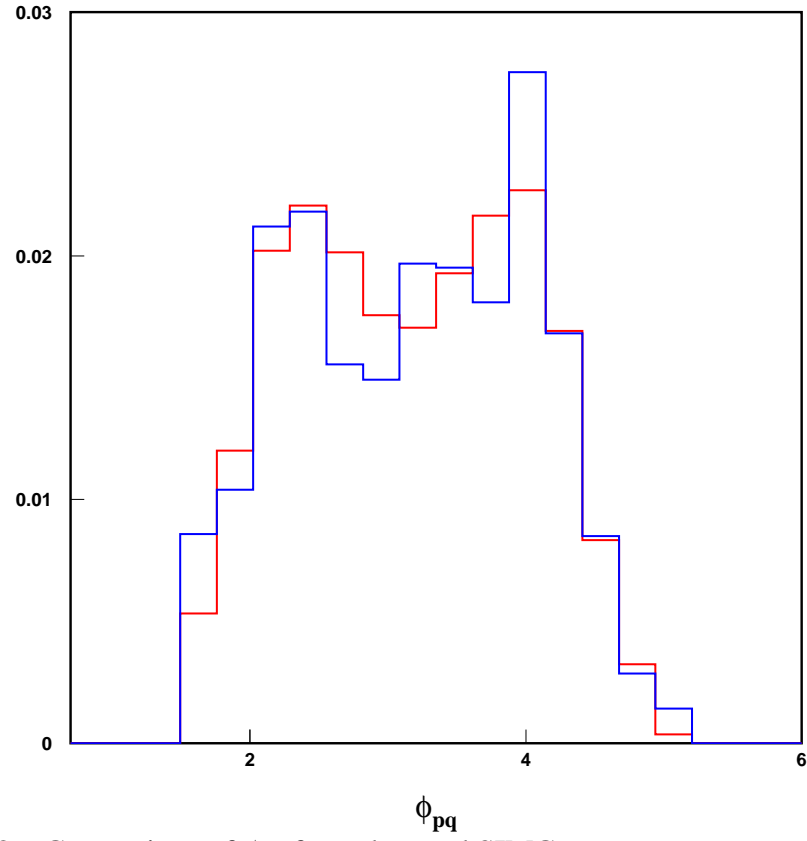


Figure 4.12 Comparison of ϕ_{pq} from data and SIMC.

ϕ_{pq} combined Λ and Σ for both SIMC and data yields in RED and BLUE, respectively, for $Q^2=2.2$ (GeV/c)².

CHAPTER 5

RESULTS

In this chapter, we will discuss the first measurement of the nucleon number A and Q^2 dependence of nuclear transparency for the $A(e, e'K^+)$ process. Nuclear transparencies for ^{12}C , ^{63}Cu and ^{197}Au nuclei over a Q^2 range of 1.1 to 3.0 $(\text{GeV}/c)^2$ are shown with the super ratio of $A > 2$ nuclei to deuterium.¹ We also extracted average effective cross section for kaons in this kinematic range. We have compared our results with the available data to date.

5.1 Transparency

The ratio of cross sections for exclusive processes from nuclei to those from nucleons is termed as Nuclear Transparency (T). The nuclear transparency was determined using the experimental charge-normalized yield, \bar{Y} divided by the charge-normalized Monte Carlo equivalent yield, \bar{Y}_{SIMC} . For a given target with nucleon number, A the nuclear transparency can be expressed as

¹Transparencies for these kinematic settings with the super ratio of $A > 1$ nuclei to hydrogen are shown in APPENDIX A.1.

$$T = \frac{\left(\bar{Y}/\bar{Y}_{\text{MC}}\right)_A}{\left(\bar{Y}/\bar{Y}_{\text{MC}}\right)_D}, \quad (5.1)$$

where the denominator is the ratio of the yields for the deuterium target.

5.1.1 Transparency with Respect to Deuterium

Hydrogen consists of just one proton, and hence we considered its cross section as a free-nucleon cross section. But for all $A > 1$ targets, we have neutrons. As deuterium has one proton and one neutron and one can produce $(K^+\Sigma^-)$ from the neutron, therefore it is more appropriate to calculate transparency with respect to deuterium.² Transparency of kaon with respect to LD_2 for three kinematics for all the targets are presented in Table 5.1. In Figure 5.1 the variation of transparency with Q^2 is shown. Different targets are shown by different colors: (RED- Carbon, GREEN- Copper and BLUE- Gold) for the three different kinematic settings of $Q^2 = 1.1, 2.2$ and 3.0 (GeV/c)^2 . In Figure 5.1, the inner bar shows the statistical uncertainty and the outer bar shows the systematic uncertainty and total uncertainty as quadrature sum of these two.

5.2 Error Calculation

In this section we briefly describe the error analysis for the statistical and systematic error in the experiment.

²The transparencies with respect to the free-space cross section are shown in APPENDIX A.1.

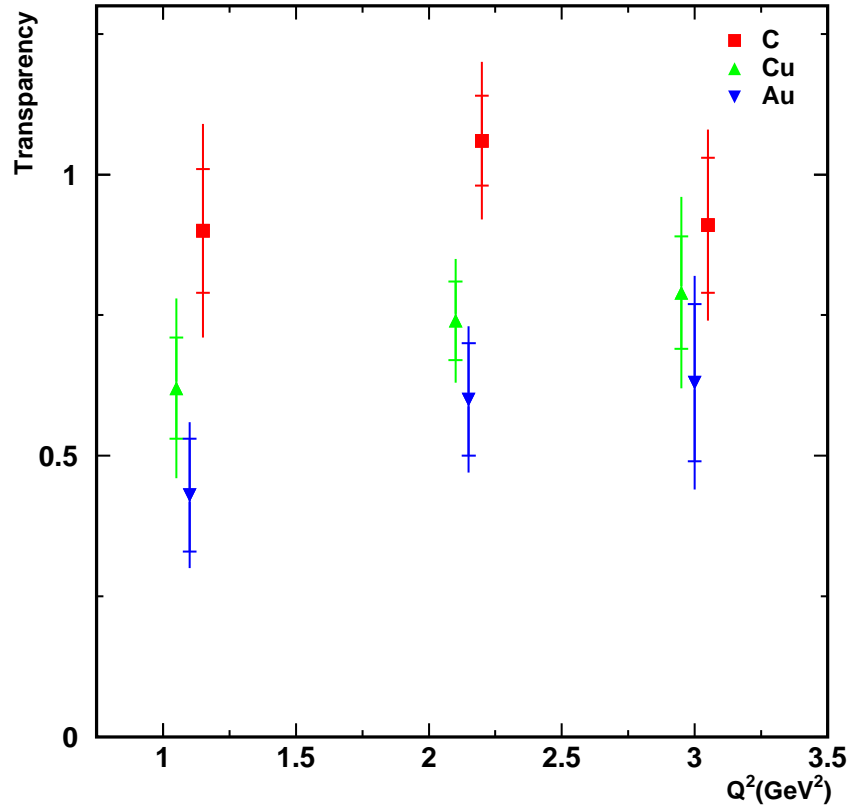


Figure 5.1 Nuclear transparency for targets of $A > 2$ with respect to LD_2 .

Carbon and copper are shifted by 0.05 and -0.05 (GeV/c)² in Q^2 , respectively, with respect to gold for convenience. The targets are shown in different colors as RED- carbon, GREEN- copper and BLUE- gold.

Table 5.1 T and σ_{eff} for different targets with respect to LD_2 .

Target	Q^2 (GeV/c) ²	Transparency	Statistical error(%)	Systematic error(%)	Total error(%)
Carbon	1.1	0.90	10.64	16.11	19.31
Copper	1.1	1.06	08.27	10.83	13.63
Gold	1.1	0.91	11.63	12.84	17.32
Carbon	2.2	0.62	09.39	12.68	15.78
Copper	2.2	0.74	07.24	07.62	10.52
Gold	2.2	0.79	10.39	13.65	17.16
Carbon	3.0	0.43	10.40	07.13	12.61
Copper	3.0	0.60	10.46	07.60	12.93
Gold	3.0	0.63	14.03	12.92	19.07

5.2.1 Statistical Error Calculation

The statistical uncertainties in the charge-normalized experimental yields were calculated for each run and summed over the runs at a given kinematic setting. The total charge-normalized yield can be written as

$$\bar{Y} = \left(\sum_i^n \frac{\bar{Y}_i}{(\bar{Y}_i/\sqrt{N_i})^2} \right) \left(\sum_i^n \frac{1}{(\bar{Y}_i/\sqrt{N_i})^2} \right)^{-1} \quad (5.2)$$

where i represents the i^{th} run of a kinematic setting and N_i is the number of events inside the experimental acceptance. The statistical uncertainty for the entire setting, $d\bar{Y}$, can be written as

$$d\bar{Y} = \left(\sum_i^n N_i/\bar{Y}_i^2 \right)^{-\frac{1}{2}} \quad (5.3)$$

We applied the same acceptance and missing mass cuts to both the experimental data and the Monte Carlo events. The Monte Carlo statistical error was determined in a similar

fashion, except N_i was replaced with the raw number of Monte Carlo particles that passed these cuts. Then statistical uncertainty in the transparency, dT_{stat} , was given by [3]

$$dT_{stat} = T \times \sqrt{\left(\left[d\bar{Y}/\bar{Y} \right]^2 + \left[d\bar{Y}_{SIMC}/\bar{Y}_{SIMC} \right]^2 \right)_A + \left(\left[d\bar{Y}/\bar{Y} \right]^2 + \left[d\bar{Y}_{SIMC}/\bar{Y}_{SIMC} \right]^2 \right)_D} \quad (5.4)$$

Table 5.2 Systematic Error.

Item	Point to Point(%)	Scale(%)	Total(%)
Particle ID	2.0	0.4- 0.7	
Charge	0.3	0.5	
Target Thickness	0.5		
Coin Blocking	0.1		
Trigger(HMS+SOS)	0.7		
Dead Time Correction	0.1		
Tracking(HMS+SOS)	0.5	0.5	
Kaon Absorption	0.5	2.0	
Beam Energy	0.1	0.1	
Cut Dependence	2.5	0.5	
Kaon Decay	0.5	1.0	
Pauli Blocking	0.5		
Radiative Correction	0.5	1.0	
Collimator	1.0		
Acceptance	0.5	2.0	
Spectral Function	1.0	2.0	
Total	3.8	3.9	5.4

5.2.2 Systematic Error Calculation

As we are using the same set of data from experiment E01-107 as used in pion transparency analysis, most of the uncertainties are same as determined during the pion trans-

parency analysis [3]. The two uncertainties that differ are uncertainty in particle identification and cut dependence. An important aspect was to investigate the stability of the results as a function of the applied cuts. The cut dependence was calculated by measuring the variation of yield due to systematic variation of the cuts. The standard deviation of the resulting yields was used as an estimate of the systematic uncertainty on the quoted yield. For different targets and different kinematic settings, uncertainties were different. List of systematic uncertainties is shown in Table 5.2.

5.3 Effective Cross Section

We can analyze the transparency results from the different nuclei and the different experiments in terms of a simple geometric model [26, 19]. This model assumes classical attenuation of protons propagating in the nucleus, with an effective nucleon-nucleon cross section σ_{eff} that is independent of density.

The effective cross section has a relation with transparency as

$$T_{hadron} = \frac{1}{Z} \int d^3r \rho_z(\vec{r}) \exp \left[- \int dz' \sigma_{eff} \rho_{A-1}(\vec{r}') \right] \quad (5.5)$$

where $\rho_z(\vec{r})$ is charge density distribution along z at \vec{r} and $\rho_{A-1}(\vec{r}')$ is at \vec{r}' for the (A-1) nucleon. Z is the number of protons. σ_{eff} is independent of density and only a free parameter in the equation.

5.3.1 Effective Cross Section of Kaons(K^+)

Kaon-nucleon effective cross section vs transparency for different targets have been plotted in Figure 5.2. We have extracted the effective cross section corresponding to the measured transparencies using these dependencies of transparency and effective cross section. For example, the measured transparency at $Q^2 = 1.1 \text{ (GeV/c)}^2$ is shown by vertical lines in Figure 5.2 and the corresponding effective cross section is shown by horizontal lines. Similarly we have calculated effective kaon-nucleon cross section for all kinematic settings which are given in Table 5.3.

Table 5.3 Effective cross section for different targets and of Q^2 for kaons

Target	Q^2 (GeV/c) ²	P_k (GeV/c)	Transparency	Effective cross section (mb)
Carbon	1.1	2.8	0.80 ± 0.07	12.91 ± 5.60
Copper	1.1	2.8	0.55 ± 0.04	15.79 ± 2.35
Gold	1.1	2.8	0.39 ± 0.04	24.56 ± 3.22
Carbon	2.2	3.2	0.91 ± 0.07	05.25 ± 4.40
Copper	2.2	3.2	0.64 ± 0.04	11.46 ± 1.39
Gold	2.2	3.2	0.51 ± 0.05	16.65 ± 2.66
Carbon	3.0	3.4	0.84 ± 0.09	09.86 ± 6.60
Copper	3.0	3.4	0.73 ± 0.07	07.71 ± 2.87
Gold	3.0	3.4	0.58 ± 0.08	13.29 ± 3.54

The average effective cross section has been calculated for different kinematic settings by weighted average over different targets, as shown in Eq. 5.6. The average effective cross sections for K^+ are listed in Table 5.4 and shown in Figure 5.3 in BLUE.

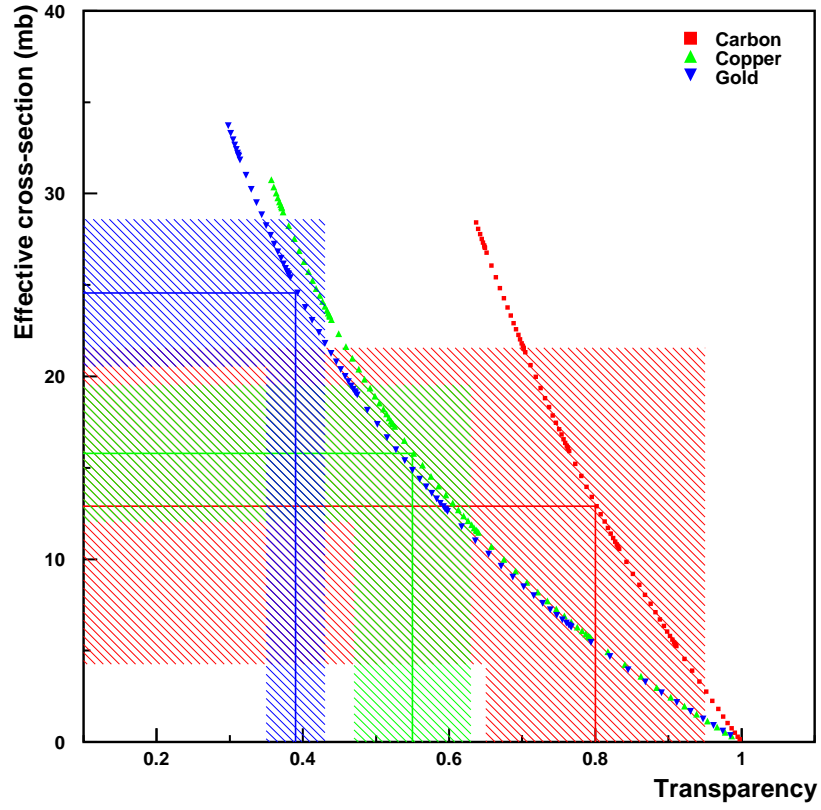


Figure 5.2 Effective cross section comparison.

Data points in RED are for carbon, GREEN data points are for copper and BLUE data points are for gold, considering only statistical uncertainty for kinematics1($Q^2=1.1$ (GeV/c) 2).

$$\sigma_{eff}^{av} = \frac{\left(1/\sigma_{err}^C\right)^2 \sigma_{eff}^C + \left(1/\sigma_{err}^{Cu}\right)^2 \sigma_{eff}^{Cu} + \left(1/\sigma_{err}^{Au}\right)^2 \sigma_{eff}^{Au}}{\left(1/\sigma_{err}^C\right)^2 + \left(1/\sigma_{err}^{Cu}\right)^2 + \left(1/\sigma_{err}^{Au}\right)^2} \quad (5.6)$$

Table 5.4 Average effective cross section for different Q^2 for kaons.

Kinematics	T_k (GeV/c)	Average effective cross section (mb)
Kin1	2.40	18.23 ± 6.87
Kin2	2.74	12.04 ± 5.33
Kin3	2.94	09.92 ± 8.02

5.3.2 Effective Cross Section of Pions (π^+)

Applying the same technique used in section 5.3.1, we have calculated the effective π^+ -nucleon cross section from the measured pion transparency [3]. The effective cross sections for different targets for five kinematic settings of $Q^2 = 1.1, 2.2, 3.0, 3.9$ and 4.7 (GeV/c)² are shown in Table 5.5. Average cross sections are listed in Table 5.6 and shown in Figure 5.3 in GREEN.

5.3.3 Effective Cross Section of Protons (p)

The average effective cross section for different kinematic settings for protons are listed in Table 5.7 from reference[8] and shown in Figure 5.3 by RED.

Table 5.5 Effective cross section for different targets and of Q^2 for pion.

Target	Q^2 (GeV/c) ²	P_k (GeV/c)	Transparency	Effective cross section (mb)
Carbon	1.1	2.8	0.67±0.01	24.82±1.12
Copper	1.1	2.8	0.45±0.01	22.34±0.75
Gold	1.1	2.8	0.28±0.01	35.99±1.38
Carbon	2.2	3.2	0.65±0.01	27.07±1.32
Copper	2.2	3.2	0.45±0.01	22.34±0.75
Gold	2.2	3.2	0.29±0.01	34.73±1.34
Carbon	3.0	3.4	0.68±0.02	23.77±2.20
Copper	3.0	3.4	0.43±0.01	23.83±0.66
Gold	3.0	3.4	0.29±0.01	34.73±1.34
Carbon	3.9	4.1	0.77±0.02	15.21±1.58
Copper	3.9	4.1	0.52±0.01	17.56±0.48
Gold	3.9	4.1	0.34±0.01	28.84±0.98
Carbon	4.7	4.4	0.70±0.03	21.67±3.00
Copper	4.7	4.4	0.53±0.02	17.20±1.21
Gold	4.7	4.4	0.33±0.02	30.23±1.38

Table 5.6 Average effective cross section for different Q^2 for pion.

Kinematics	T_k (GeV/c)	Average effective cross section (mb)
Kin1	2.8	25.29±1.93
Kin2	3.2	25.64±2.02
Kin3	3.4	25.81±2.66
Kin4	4.1	19.43±1.92
Kin5	4.4	22.76±3.52

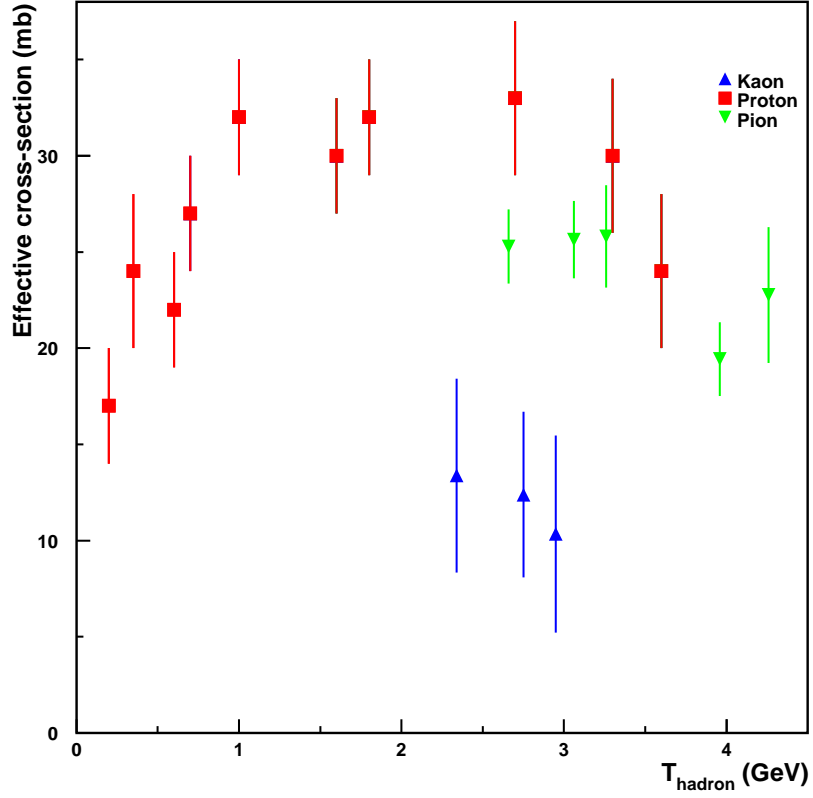


Figure 5.3 Effective cross section vs transparency.

Data points in RED is for protons, GREEN data points are for π^+ and BLUE data points are from this analysis for K^+ , considering only statistical uncertainty [34].

Table 5.7 Average effective cross section for different T_K for protons[17].

Kinematics	T_k (GeV/c)	Average effective cross section (mb)
Kin1	0.20	17 ± 3
Kin2	0.35	24 ± 4
Kin3	0.60	22 ± 3
Kin4	0.70	27 ± 3
Kin5	1.00	32 ± 3
Kin6	1.60	30 ± 3
Kin7	1.80	32 ± 3
Kin8	2.70	33 ± 4
Kin9	3.30	30 ± 4
Kin10	3.60	24 ± 4
Kin11	4.30	33 ± 3

5.3.4 Effective Cross Section for All Hadrons (π^+ , K^+ , p)

The world data [6] on p-p, p-n total cross sections as a function of kinetic energy (T_{hadron}) was fitted to a function form as shown in Figure 5.4. The error bars are statistical only. T_{hadron} is defined as

$$T_{hadron} = \sqrt{P_{hadron}^2 + M_{hadron}^2} - M_{hadron} \quad (5.7)$$

We also performed similar fits for the world π^+ -p, π^+ -n and K^+ -p, K^+ -n data as shown in Figure 5.4. We then compared the effective cross section extracted from our experiment to these fitted forms for the proton, pion and kaon. The results are shown in Figure 5.5 with RED for protons, GREEN for pions and BLUE for kaons.

Note that the world data of hadron-nucleon scattering cross sections are obtained from hadron scattering experiments. In this analysis, we compared the electron scattering effective cross section with those obtained from hadron-scattering experiments.

Table 5.8 Scale factors for different hadron-nucleon scattering.

Scattering	Scale factor
p -p	0.67
π^+ -p	0.91
K^+ -p	0.59
p -n	0.67
π^+ -n	0.91
K^+ -n	0.59

The scale factors in Table 5.8 indicate the differences in the nature of the probes used: electromagnetic for electrons vs strong for hadrons. Since the electromagnetic interaction is weaker than the strong interaction, hence electrons can probe deeper into the nucleus compare to hadrons. This leads the scale factors between electron-scattering and hadron-scattering technique. The remarkable agreement between the K.E. dependence of the proton cross sections obtained from electron scattering and hadron scattering point to the similar reaction mechanisms that are well described within traditional nuclear physics. The deviation of the pion results indicate a break down of traditional nuclear physics reaction mechanisms for pions. For the kaons, our uncertainties are too large to draw any conclusions.

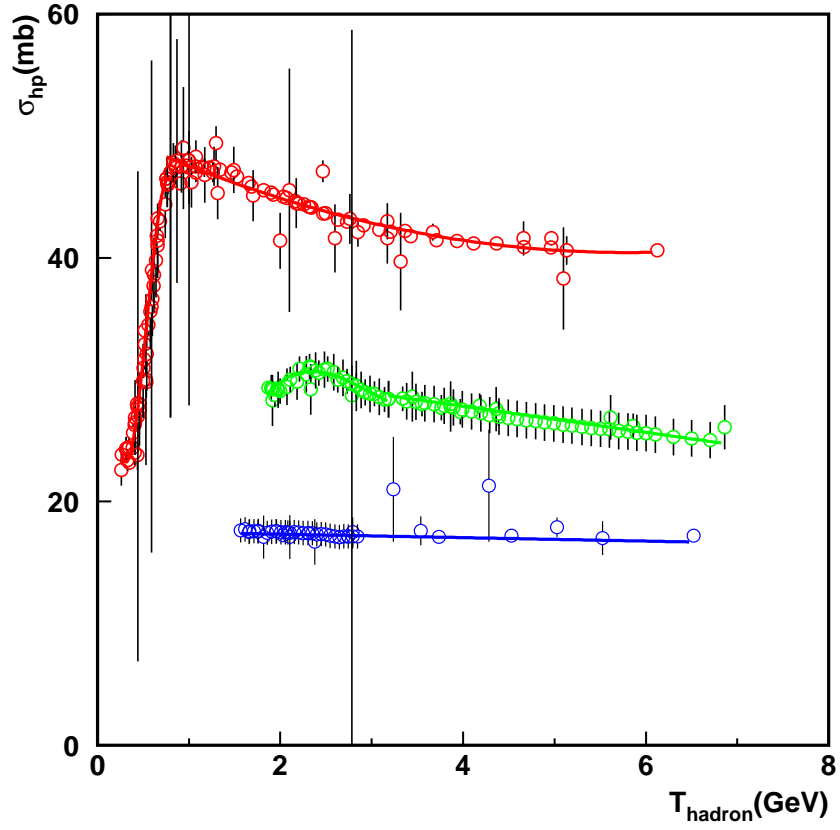


Figure 5.4 Hadron-proton total cross section vs T_{hadron} .

Data points in RED are for protons, GREEN data points are for π^+ and BLUE data points are from this analysis for K^+ from [34].

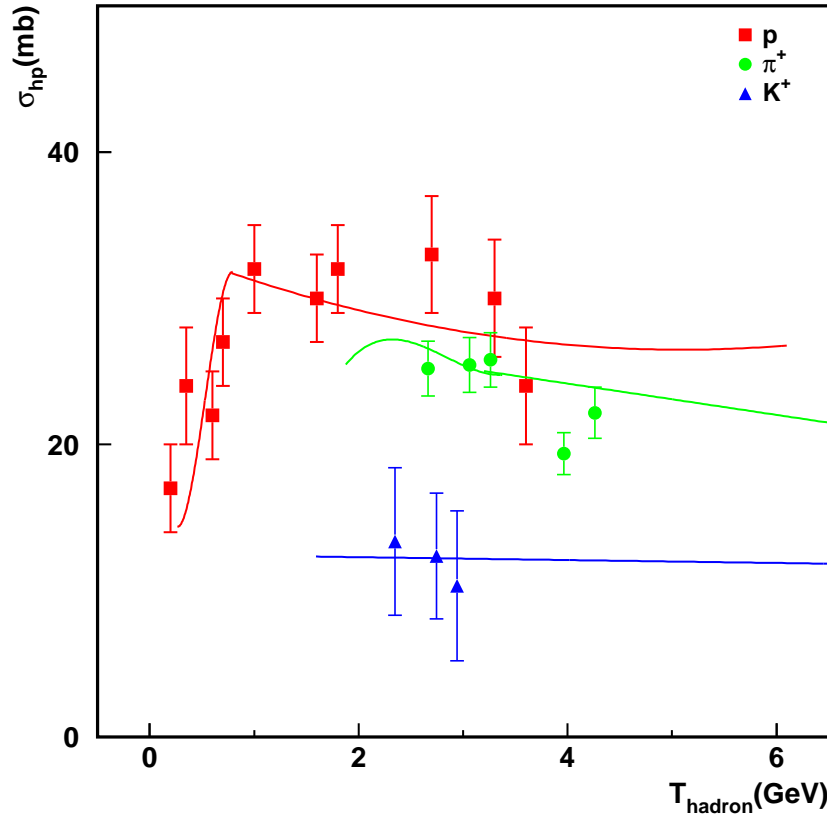


Figure 5.5 Comparison of effective and hadron-proton total cross section.

Data points in RED are for protons from [34], GREEN data points are for π^+ and BLUE data points are from this analysis for K^+ . The fits are from hadron-scattering world data[6] with scale factors given in Table 5.8.

5.3.5 A Dependency of Transparency

The A dependence of the nuclear transparency is extracted from the simple ansatz $T = A^{1-\alpha}$, where α is used to parametrize the nuclear cross section and σ_N is in terms of the elementary nucleon cross-section, σ_0 as $\sigma_N = \sigma_0 A^\alpha$.

Table 5.9 α values for different Q^2 for kaons with respect to LD_2 .

Kinematics	Q^2 (GeV/c) ²	α
Kin1	1.1	0.84±0.06
Kin2	2.2	0.91±0.04
Kin3	3.0	0.92±0.05

The Q^2 dependence of nuclear transparency was very small for the kinematics range of $Q^2 = 1.1$ (GeV/c)² to $Q^2 = 3.0$ (GeV/c)². Fitting the transparency for a particular Q^2 to $T = A^{1-\alpha}$, we get α as shown in Table 5.9.³ We extracted transparency and effective cross section for different kinematic settings for kaons in this analysis and calculated effective cross sections for available transparencies for protons and pions. α values have been plotted against effective cross section from this work and reference [17] in Figure 5.6.

The results indicate that the effective cross section obtained from electron-scattering is smaller than hadron-scattering (as expected from the nature of the probe). For protons and pions, the parameter α extracted from electro-production measurements do not agree with those obtained from hadro-production, some of these differences may also be related to the strength of the interaction between the incident hadron and the nucleons. For kaons,

³The value of α with respect to hydrogen is given in APPENDIX A, Table B.1.

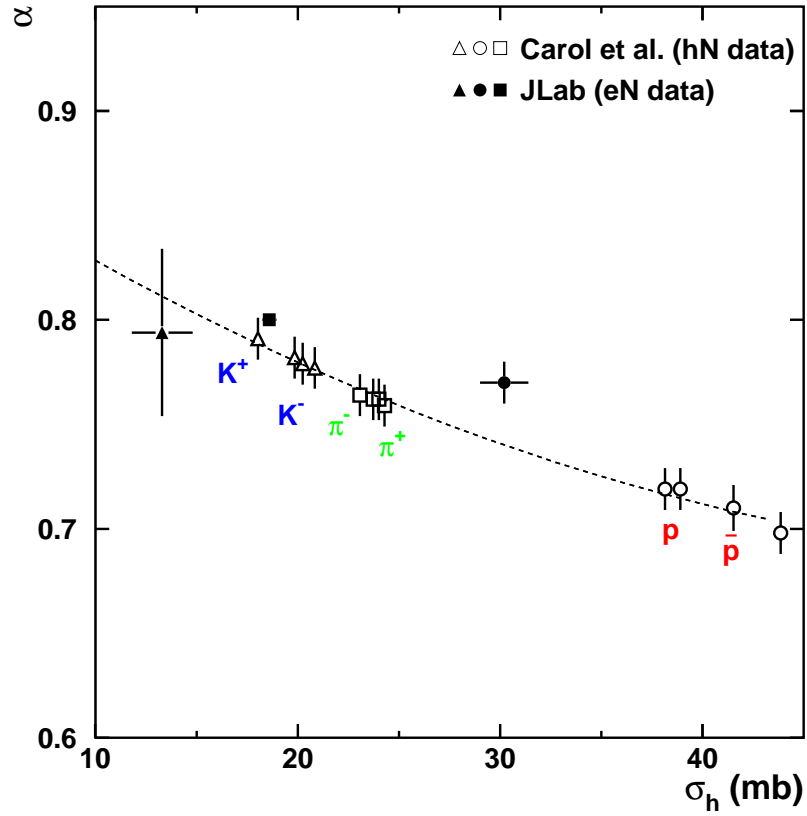


Figure 5.6 α from electro-production of hadrons and from hadron-scattering.

α from electro-production of kaons (from this analysis), pions, and protons are shown by solid triangle, square, and circle, respectively. Similarly, α from hadron-scattering reactions are shown by empty points and fitted with dotted curve [8].

the parameter α from electro-production is consistent within statistical uncertainties, with those obtained from hadro-production. However, due to the low statistics of kaons in our data set, we cannot draw any strong conclusions.

CHAPTER 6

CONCLUSIONS

6.1 Conclusions

The nuclear transparency of kaons in the reaction $A(e, e'K^+)$ was measured by forming a super ratio of the experimental yield to the Monte Carlo simulation yield from ^{12}C , ^{63}Cu and ^{197}Au to the yields from ^2H at $Q^2 = 1.1, 2.2$ and 3.0 (GeV/c)^2 . Both the energy and A dependence of the nuclear transparency are consistent with traditional nuclear physics expectations within experimental errors.

The effective kaon-nucleon cross sections extracted from the nuclear transparency are also consistent with the world data on hadron-scattering. The electromagnetic interaction is weaker than the strong interaction, hence electrons can probe deeper into the nucleus compared to hadrons. This manifests as a scale factor between the effective hadron-nucleon cross sections extracted from electro-production vs hadro-production measurements. The magnitude of these scale factors are an excellent measure of the differences in the propagation of nucleons vs mesons in the nuclear medium.

For protons and pions, the A dependence of the nuclear transparency, (parameterized as α), extracted from electro-production measurements do not agree with those obtained from hadro-production. Some of these discrepancy can be also explained in terms of the differences in the probes used.

For kaons, the α extracted from our electro-production data are consistent within statistical uncertainties, with the hadro-production results. However, given the large statistical uncertainties of our results, we are unable to draw any strong conclusions.

This analysis adds to our understanding of kaon propagation in the nuclear medium and will help improve the design of future kaon electro-production experiments aimed at studying the reaction mechanisms.

6.2 Further Research

In the future, JLab will upgrade its energy from 6 GeV to 12 GeV and the nuclear transparency effect will be probed at higher Q^2 compared to previous experiments. Experiment E12-06-107 aims to confirm the onset of CT in pions and search for CT in protons. Studies of hadronization in nuclei by deep inelastic scattering and L-T separated kaon electro-production cross section from 5-11 GeV will be performed by experiments E12-07-101 and E12-09-011, respectively. We hope these experiments will give us a better understanding of the reaction mechanism of kaon electro-production and kaon propagation through nuclei.

REFERENCES

- [1] D. Abbott, A. Ahmidouch, T. A. Amati, C. Armstrong, J. Arrington, K. A. Assamagan, K. Bailey, O. K. Baker, S. Barrow, K. Beard, D. Beatty, S. Beedoe, E. Beise, E. Belz, C. Bochna, H. Breuer, E. E. W. Bruins, R. Carlini, J. Cha, N. Chant, C. Cothran, W. J. Cummings, S. Danagoulian, D. Day, D. DeSchepper, J.-E. Ducret, and F. Duncan, “Quasifree $(e, e'p)$ Reactions and Proton Propagation in Nuclei,” *Phys. Rev. Lett.*, vol. 80, no. 23, Jun 1998, pp. 5072–5076.
- [2] S. V. Akulinichev, “Pion contribution to K^+ -nucleus scattering,” *Phys. Rev. Lett.*, vol. 68, no. 3, Jan 1992, pp. 290–292.
- [3] Benjamin Micheal Patrick Clasio, *Measurement of Nuclear Transparency from $A(e, e'\pi^+)$ Reactions*, *PhD Thesis*, MASSACHUSETTS INSTITUTE OF TECHNOLOGY, 2006.
- [4] G. E. Brown, C. B. Dover, P. B. Siegel, and W. Weise, ,” *Phys. Rev. Lett.*, vol. 26, no. 2723, 1988.
- [5] D. V. Bugg, R. S. Gilmore, K. M. Knight, D. C. Salter, G. H. Stafford, E. J. N. Wilson, J. D. Davies, J. D. Dowell, P. M. Hattersley, R. J. Homer, A. W. O’dell, A. A. Carter, R. J. Tapper, and K. F. Riley, “Kaon-Nucleon Total Cross Sections from 0.6 to 2.65 GeV/c,” *Phys. Rev.*, vol. 168, no. 5, Apr 1968, pp. 1466–1475.
- [6] C. Amsler et al.(Particle Data Group) PL B667, 1, (2008) and 2009 partial update for the 2010 edition(URL: <http://pdg.lbl.gov>).
- [7] J. C. Caillon and J. Labarsouque, “ K^+ -nucleus cross sections with a density-dependent $K+N$ interaction,” *Phys. Rev. C.*, vol. 45, no. 5, May 1992, pp. 2503–2506.
- [8] A. S. Carroll, I. H. Chiang, T. F. Kycia, K. K. Li, M. D. Marx, D. C. Rahm, W. F. Baker, D. P. Eartly, G. Giacomelli, A. M. Jonckheere, P. F. M. Koehler, P. O. Mazur, R. Rubinstein, and O. Fackler, “Total cross sections of π , K , p and on protons and deuterons between 200 and 370 (GeV/c),” *Phys. Lett. B.*, vol. 80, no. 4-5, 1979, pp. 423 – 427.
- [9] C. M. Chen, D. J. Ernst, and M. B. Johnson, “High-energy pion-nucleus elastic scattering,” *Phys. Rev. C*, vol. 48, no. 2, Aug 1993, pp. 841–849.

- [10] B. Clasie, X. Qian, J. Arrington, R. Asaturyan, F. Benmokhtar, W. Boeglin, P. Bosted, A. Bruell, M. E. Christy, E. Chudakov, W. Cosyn, M. M. Dalton, A. Daniel, D. Day, D. Dutta, L. El Fassi, R. Ent, H. C. Fenker, J. Ferrer, N. Fomin, H. Gao, K. Garrow, D. Gaskell, C. Gray, T. Horn, G. M. Huber, M. K. Jones, and *et. al.*, “Measurement of Nuclear Transparency for the $A(e, e'\pi^+)$ Reaction,” *Phys. Rev. Lett.*, vol. 99, no. 24, Dec 2007, p. 242502.
- [11] David J. Gaskell, *Longitudinal Electroproduction of Charged Pions from Hydrogen, Deuterium and Helium-3*, *PhD Thesis*, Oregon State University, <http://www1.jlab.org/UL/publications/documents/gaskell.pdf>, 2001.
- [12] C. B. Dover and P. J. Moffa, “Interaction of K^+ mesons with nuclei,” *Phys. Rev. C*, vol. 16, no. 3, Sep 1977, pp. 1087–1096.
- [13] D. Dutta, “Experimental search for color transparency at Jefferson Lab,” *Eur. Phys. J.*, vol. A19S1, 2004, pp. 179–183.
- [14] R. Ent, B. W. Filippone, N. C. R. Makins, R. G. Milner, T. G. O’Neill, and D. A. Wasson, “Radiative corrections for $(e, e'p)$ reactions at GeV energies,” *Phys. Rev. C*, vol. 64, no. 5, Oct 2001, p. 054610.
- [15] C. Garcia-Recio, J. Nieves, and E. Oset, “Pion cloud contribution to K^+ -nucleus scattering,” *Phys. Rev. C*, vol. 51, no. 1, Jan 1995, pp. 237–251.
- [16] G. Garino, M. Saber, R. E. Segel, D. F. Geesaman, R. Gilman, M. C. Green, R. J. Holt, J. P. Schiffer, B. Zeidman, E. J. Beise, G. W. Dodson, S. Høibråten, L. D. Pham, R. P. Redwine, W. W. Sapp, C. F. Williamson, S. A. Wood, N. S. Chant, P. G. Roos, J. D. Silk, M. Deady, and X. K. Maruyama, “Proton propagation in nuclei studied in the $(e, e'p)$ reaction,” *Phys. Rev. C*, vol. 45, no. 2, Feb 1992, pp. 780–790.
- [17] K. Garrow, D. McKee, A. Ahmidouch, C. S. Armstrong, J. Arrington, R. Asaturyan, S. Avery, O. K. Baker, D. H. Beck, H. P. Blok, C. W. Bochna, W. Boeglin, P. Bosted, M. Bouwhuis, H. Breuer, D. S. Brown, A. Bruell, R. D. Carlini, N. S. Chant, A. Cochran, L. Cole, S. Danagouliau, D. B. Day, J. Dunne, D. Dutta, R. Ent, H. C. Fenker, and *et. al.*, “Nuclear transparency from quasielastic $A(e, e'p)$ reactions up to $Q^2 = 8.1(\text{GeV}/c)^2$,” *Phys. Rev. C*, vol. 66, no. 4, Oct 2002, p. 044613.
- [18] <http://www.jlab.org/>.
- [19] P. Jain and J. Ralston, “Systematic analysis method for color transparency experiments,” *Phys. Rev. D*, vol. 48, no. 3, Aug 1993, pp. 1104–1111.
- [20] Jiang, M. F. Koltun, and D. S., “Meson exchange current contribution to K^+ -nucleus scattering,” *Phys. Rev. C*, vol. 46, no. 6, Dec 1992, pp. 2462–2475.
- [21] M. J. Jiang, D. J. Ernst, and C. M. Chen, ,” *Phys. Lett. C.*, vol. 51, no. 857, 1995.

- [22] C. W. Leemann, D. R. Douglas, and G. A. Krafft, “Radiative corrections for $(e, e'p)$ reactions at GeV energies,” *Ann. Rev. Nucl. Part. Sci.*, vol. 51, no. 413, 2001.
- [23] N. C. R. Makins, R. Ent, M. S. Chapman, J.-O. Hansen, K. Lee, R. G. Milner, J. Nelson, R. G. Arnold, P. E. Bosted, C. E. Keppel, A. Lung, S. E. Rock, M. Spengos, Z. M. Szalata, L. H. Tao, J. L. White, K. P. Coulter, D. F. Geesaman, R. J. Holt, H. E. Jackson, V. Papavassiliou, D. H. Potterveld, B. Zeidman, J. Arrington, E. J. Beise, E. Belz, and B. W. Filippone, “Momentum transfer dependence of nuclear transparency from the quasielastic $C^{12}(e, e'p)$ reaction,” *Phys. Rev. Lett.*, vol. 72, no. 13, Mar 1994, pp. 1986–1989.
- [24] Y. Mardor, E. Piasetsky, J. Alster, D. Ashery, M. A. Moinester, A. I. Yavin, S. Bart, R. E. Chrien, P. H. Pile, R. J. Sutter, R. A. Krauss, J. C. Hiebert, R. L. Stearns, T. Kishimoto, R. R. Johnson, and R. Olshevsky, “ K^+ total cross sections as a test for nucleon “swelling”,” *Phys. Rev. Lett.*, vol. 65, no. 17, Oct 1990, pp. 2110–2113.
- [25] D. Marlow, P. D. Barnes, N. J. Colella, S. A. Dytman, R. A. Eisenstein, R. Grace, F. Takeuchi, W. R. Wharton, S. Bart, D. Hancock, R. Hackenberg, E. Hungerford, W. Mayes, L. Pinsky, T. Williams, R. Chrien, H. Palevsky, and R. Sutter, “Kaon scattering from C and Ca at 800 MeV/c,” *Phys. Rev. C*, vol. 25, no. 5, May 1982, pp. 2619–2637.
- [26] T. G. O’Neill, W. Lorenzon, P. Anthony, R. G. Arnold, J. Arrington, E. J. Beise, J. E. Belz, P. E. Bosted, H. J. Bulten, M. S. Chapman, K. P. Coulter, F. Dietrich, R. Ent, M. Epstein, B. W. Filippone, H. Gao, R. A. Gearhart, D. F. Geesaman, J. O. Hansen, R. J. Holt, H. E. Jackson, C. E. Jones, C. E. Keppel, E. R. Kinney, S. Kuhn, K. Lee, A. Lung, N. C. R. Makins, D. J. Margaziotis, R. D. McKeown, R. G. Milner, B. Mueller, J. Napolitano, J. Nelson, V. Papavassiliou, G. G. Petratos, D. H. Potterveld, S. E. Rock, M. Spengos, Z. M. Szalata, L. H. Tao, K. van Bibber, J. F. J. van den Brand, J. L. White, and B. Zeidman, “A-dependence of nuclear transparency in quasielastic $A(e, e'p)$ at high 2,” *Phys. Lett. B*, vol. 351, no. 1 - 3, 1995, pp. 87 – 92.
- [27] M. J. Paez and R. H. Landau, “Nuclear structure effects in k^+ elastic scattering from ^3He , ^3H , ^4He , and ^{12}C ,” *Phys. Rev. C*, vol. 24, no. 3, Sep 1981, pp. 1120–1134.
- [28] X. Qian, T. Horn, B. Clasie, J. Arrington, R. Asaturyan, F. Benmokhtar, W. Boeglin, P. Bosted, A. Bruell, M. E. Christy, E. Chudakov, M. M. Dalton, A. Daniel, D. Day, D. Dutta, L. El Fassi, R. Ent, H. C. Fenker, J. Ferrer, N. Fomin, H. Gao, K. Garrow, D. Gaskell, C. Gray, G. M. Huber, M. K. Jones, N. Kalantarians, and *et. al.*, “Experimental study of the $A(e, e'\pi^+)$ reaction on ^1H , ^2H , ^{12}C , ^{27}Al , ^{63}Cu , and ^{197}Au ,” *Phys. Rev. C*, vol. 81, no. 5, May 2010, p. 055209.
- [29] Richard Matthew Mohring, *A Comparison of Longitudinal and Transverse Cross Section in the Reactions $p(e, e'K^+)\Lambda$ and $p(e, e'K^+)\Sigma$ Reactions*, *PhD Thesis*, University of Maryland, 1999.

- [30] R. Sawafta, R. Weiss, J. Aclander, J. Alster, M. Barakat, S. Bart, R. E. Chrien, R. A. Krauss, K. Johnston, I. Mardor, Y. Mardor, S. MayTal-Beck, E. Piasetzky, P. H. Pile, H. Seyfarth, R. L. Stearns, R. J. Sutter, and I. A. Yavin, “The influence of the nuclear medium on K^+ total cross sections,” *Physics Letters B*, vol. 307, no. 3-4, 1993, pp. 293 – 297.
- [31] P. B. Siegel, W. B. Kauffmann, and W. R. Gibbs, “ K^+ -nucleus elastic scattering and charge exchange,” *Phys. Rev. C.*, vol. 30, no. 4, Oct 1984, pp. 1256–1266.
- [32] P. B. Siegel, W. B. Kaufmann, and W. R. Gibbs, “ K^+ as a probe of partial deconfinement in nuclei,” *Phys. Rev. C*, vol. 31, no. 6, Jun 1985, pp. 2184–2189.
- [33] R. Weiss, J. Aclander, J. Alster, M. Barakat, S. Bart, R. E. Chrien, R. A. Krauss, K. Johnston, I. Mardor, Y. Mardor, S. May Tal-beck, E. Piasetzky, P. H. Pile, R. Sawafta, H. Seyfarth, R. L. Stearns, R. J. Sutter, and A. I. Yavin, “Measurement of low energy K^+ total cross sections on $N=Z$ nuclei,” *Phys. Rev. C.*, vol. 49, no. 5, May 1994, pp. 2569–2577.
- [34] Wendy L. Hinton, *Quasifree Electroproduction of Λ , Σ^0 , and Σ^- Hyperons on Carbon and Aluminium*, *PhD Thesis*, Hampton University, May 2001.

APPENDIX A
TRANSPARENCY WITH HYDROGEN

A.1 Transparency with Respect to Hydrogen

Transparency of kaon with respect to free-nucleon cross section for three kinematics for all the targets is shown in Table A.2. We used hydrogen cross section as the free-nucleon cross section. The total uncertainty has been taken as the quadrature sum of the statistical and systematic uncertainty. The different targets are shown by different colors as: BLACK- LD_2 , RED- carbon, GREEN- copper and BLUE- gold for three different kinematics ($Q^2 = 1.1, 2.2$ and 3.0 (GeV/c)²). In Figure A.1, the inner bar shows the statistical uncertainty and outer bar shows the systematic uncertainty and total uncertainty as quadrature sum these two.

Table A.1 Cross section for hydrogen for different Q^2 for kaons.

Q^2 (GeV/c) ²	P_K (GeV/c)	Cross section (mb)	Statistical error(%)	Systematic error(%)	Total error(%)
1.1	2.8	9.46	6.28	5.61	8.42
2.2	3.2	8.72	4.76	4.41	6.49
3.0	3.4	9.29	7.44	4.89	8.91

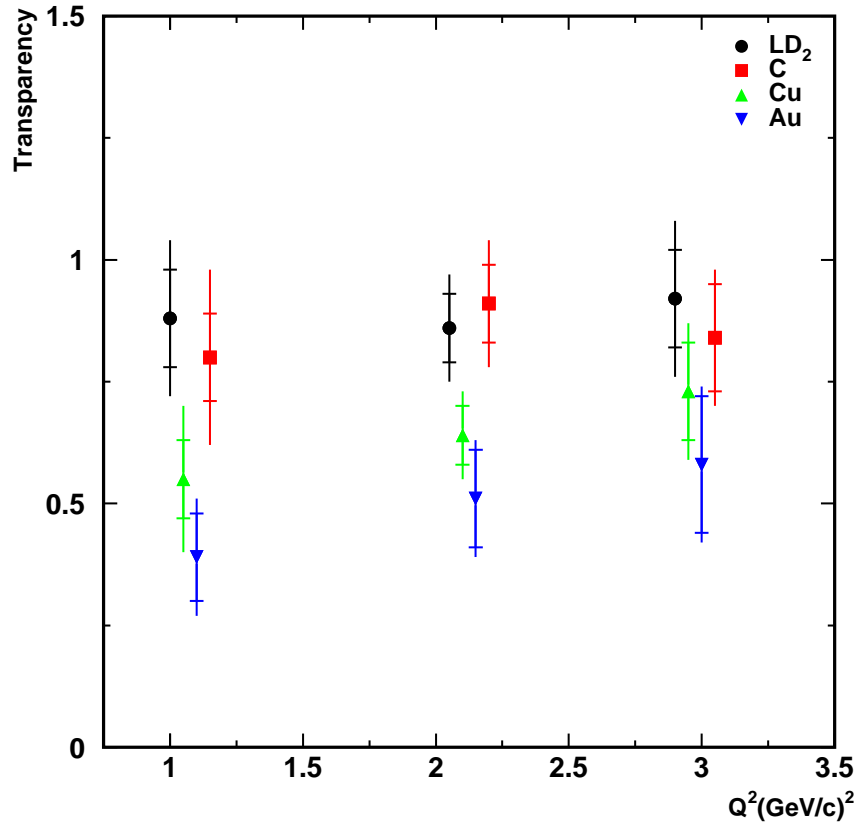


Figure A.1 Nuclear transparency with respect to H_2 target.

Copper, carbon and LD_2 are shifted by -0.05 , 0.05 and $-0.10 (\text{GeV}/c)^2$ in Q^2 , respectively, for convenience.

Table A.2 T and σ_{eff} for different targets with respect to H_2 .

Target	Q^2 (GeV/c) ²	Cross section (mb)	Transparency	Statistical error(%)	Systematic error(%)	Total error(%)
LD_2	1.1	8.38	0.88	10.30	12.34	16.07
Carbon	1.1	7.57	0.80	09.31	16.11	18.61
Copper	1.1	5.17	0.55	07.85	12.69	14.92
Gold	1.1	3.64	0.39	09.03	07.13	11.51
LD_2	2.2	7.53	0.86	07.51	07.48	10.61
Carbon	2.2	8.01	0.91	07.58	10.03	12.57
Copper	2.2	5.60	0.64	06.45	06.43	09.11
Gold	2.2	4.49	0.51	09.93	06.40	11.82
LD_2	3.0	8.55	0.92	10.22	12.06	15.81
Carbon	3.0	7.76	0.84	11.49	08.10	14.06
Copper	3.0	6.75	0.73	10.24	09.33	13.85
Gold	3.0	5.42	0.58	13.91	08.22	16.16

Table A.3 Cross section for deuterium for different Q^2 for kaons.

Q^2 (GeV/c) ²	P_K (GeV/c)	Cross section (mb)	Statistical error(%)	Systematic error(%)	Total error(%)
1.1	2.8	8.38	8.14	10.68	13.43
2.2	3.2	7.53	5.80	06.03	08.37
3.0	3.4	8.55	7.34	11.06	13.27

APPENDIX B
MISCELLANEOUS

B.1 α Plot

We have shown α for three kinematic settings in Table B.1 plotted in BLUE in Figure B.1 with respect to hydrogen target. The available α values from proton and pion analysis have been shown in RED and GREEN, respectively, for comparison. We considered only the statistical uncertainties which are shown by closed vertical lines. The experimental α values from the processes other than electro-production are shown by the horizontal band in Figure B.1. The width of the band represents statistical uncertainty.

Table B.1 α values for different Q^2 for kaons with respect to hydrogen.

Kinematics	Q^2 (GeV/c) ²	α
Kin1	1.1	0.84 ± 0.06
Kin2	2.2	0.91 ± 0.04
Kin3	3.0	0.92 ± 0.05

B.2 Comparison of Yields for Data with SIMC

We already discussed in section 4.4 about the dependency of the cross section upon four variables: Q^2 , W , t and ϕ_{pq} , where Q^2 is four-momentum transferred square, W is the center of mass energy, t is momentum transfer, and ϕ_{pq} is the angle between the scattering and reaction planes. In this appendix, we are showing comparison of SIMC and data yields for missing mass, W , t and ϕ_{pq} in the Figure B.2, Figure B.3, Figure B.4 and Figure B.5, respectively. We have already shown the comparison for Q^2 in section 4.4.

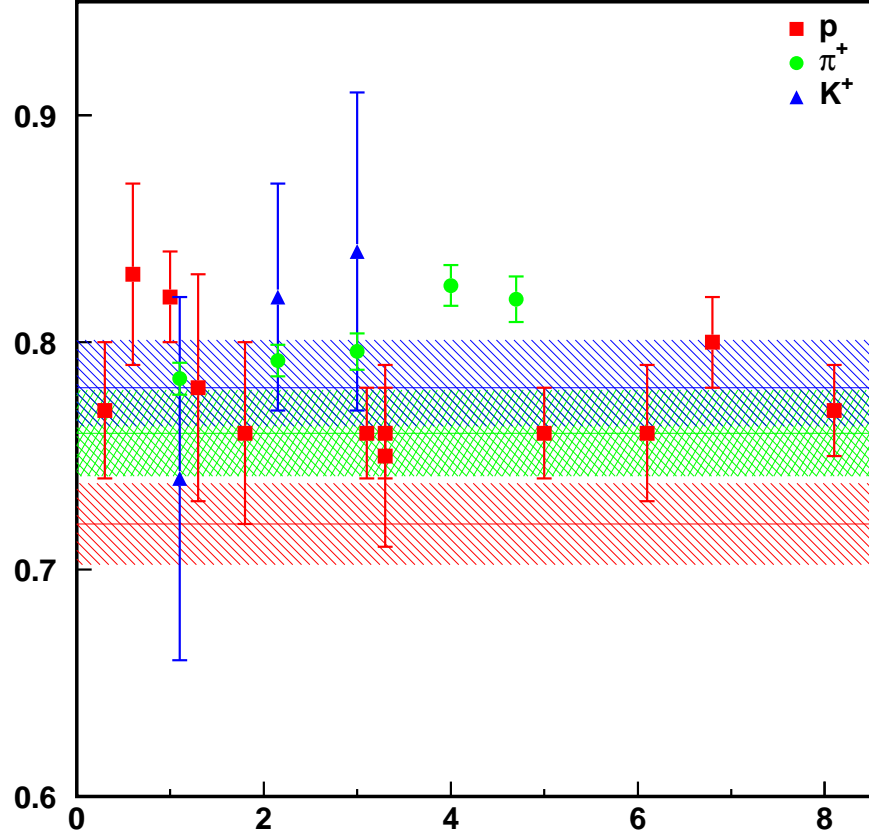


Figure B.1 α for different kinematics electro-production and hadro-production.

Electro-production data points in RED are for protons, GREEN data points are for π^+ and BLUE data points are from this analysis for K^+ . Similarly, horizontal lines corresponds to α values from hadron-scattering with error band for different hadrons.

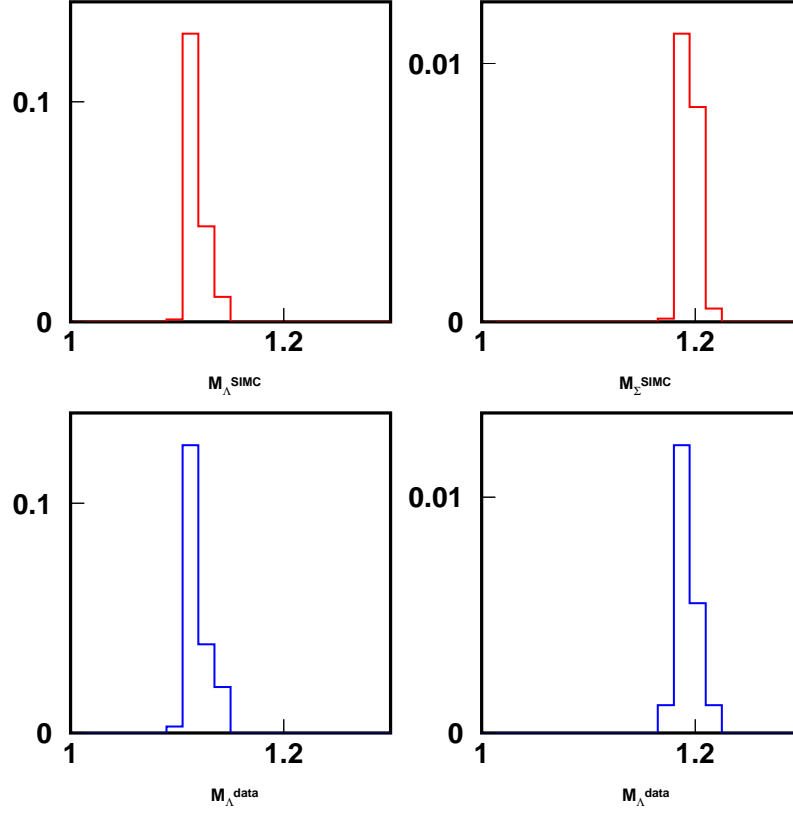


Figure B.2 Missing mass are shown here after applying cuts.

One-dimensional plot of missing mass are shown here after applying all the cuts. Clockwise top left corner: M_{Λ}^{SIMC} and M_{Σ}^{SIMC} in RED, M_{Σ}^{data} and M_{Λ}^{data} in BLUE for $Q^2=2.2 \text{ (GeV/c)}^2$.

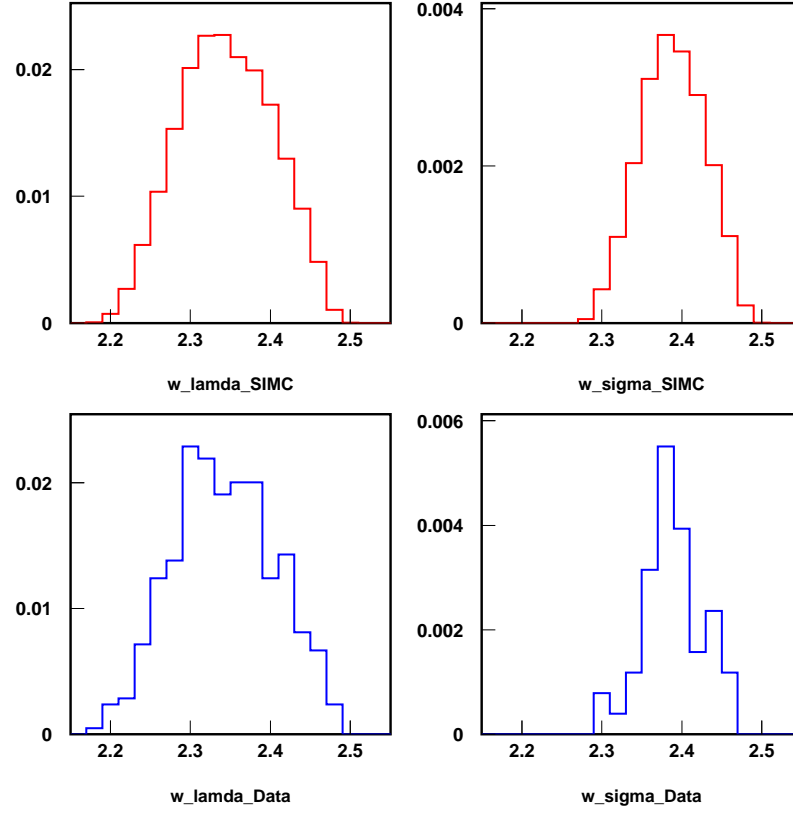


Figure B.3 Comparison of W from data and SIMC.

Clockwise from top left corner: W_Λ and W_Σ SIMC in RED, W_Σ and W_Λ data in BLUE for $Q^2=2.2$ (GeV/c)².

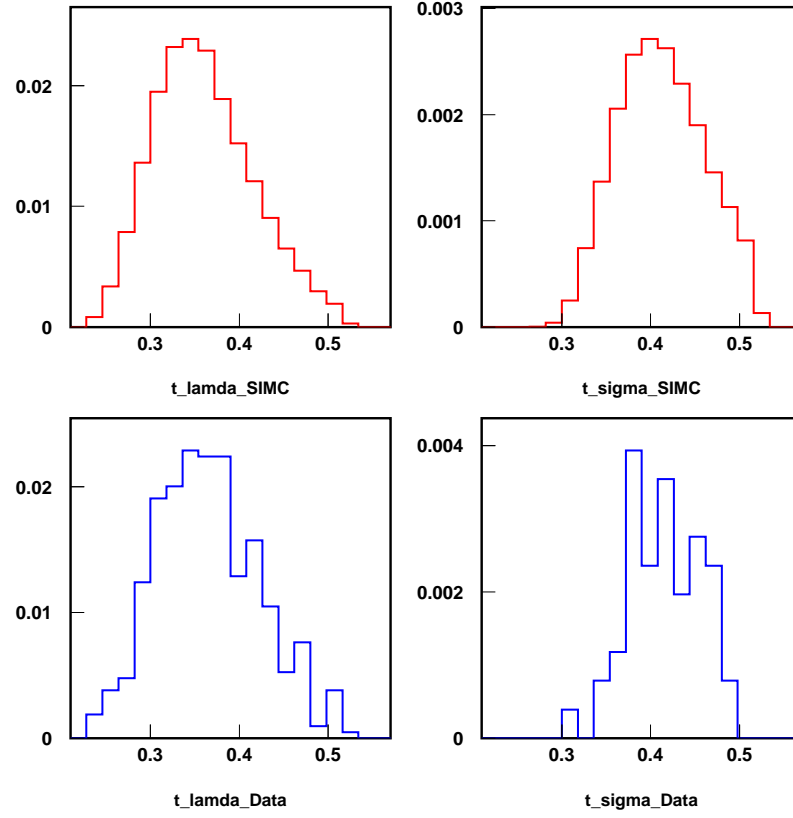


Figure B.4 Comparison of t from data and SIMC.

Clockwise from top left corner: t_{Λ} and t_{Σ} SIMC in RED, t_{Σ} data and t_{Λ} data in BLUE for $Q^2=2.2$ (GeV/c)².

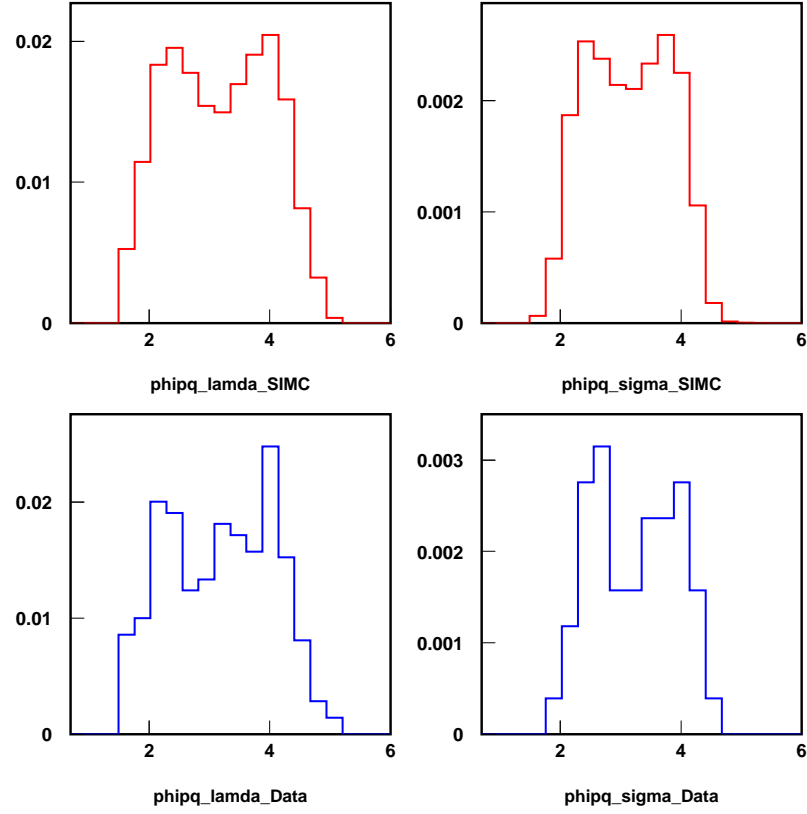


Figure B.5 Comparison of ϕ^{pq} from data and SIMC.

Clockwise from top left corner: ϕ_{Λ}^{pq} and ϕ_{Σ}^{pq} SIMC shown in RED, ϕ_{Σ}^{pq} data and ϕ_{Λ}^{pq} data in BLUE for $Q^2=2.2 \text{ (GeV/c)}^2$.

B.3 Iteration

We have done the iteration on the data to verify our transparency results. As the statistics was very low, we did not expect a large variation in the results. We fitted data for the variables Q^2 , W and t for Λ and Σ production as shown in Figure B.6, Figure B.7 and Figure B.8, respectively. These fit functions were used to generate the SIMC ntuples. New ntuples were used again for extraction of transparency to check the stability of the yields. This process was repeated doing a second iteration. After the iteration, we did not get any reasonable change in the yields and hence results presented in this thesis are without considering any iteration.

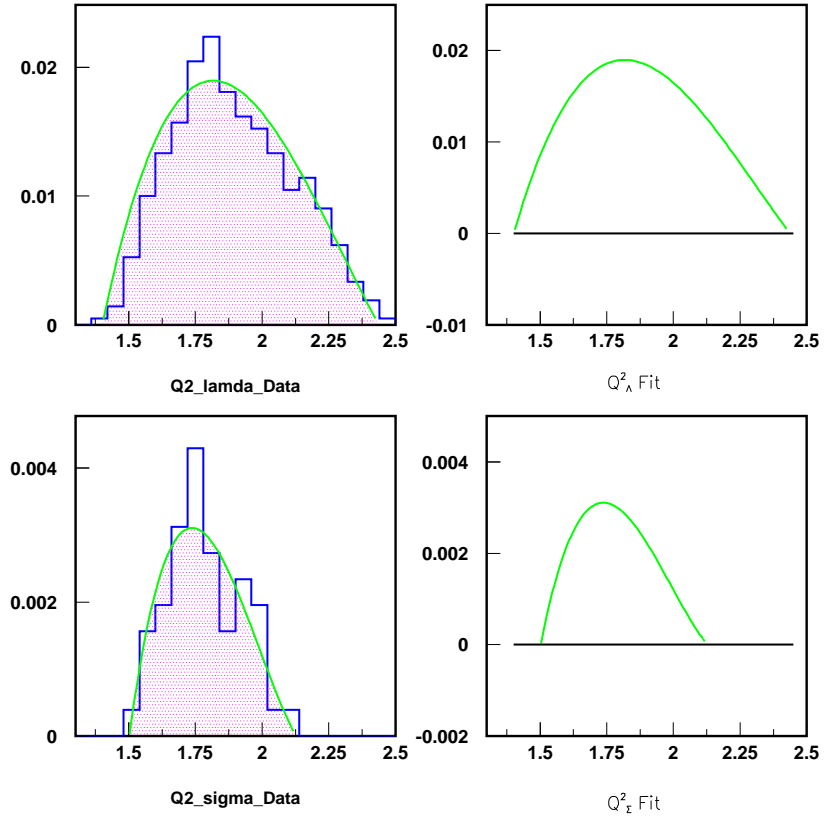


Figure B.6 Fitting the Q^2 data for kinematic settings of $Q^2=2.2 \text{ (GeV/c)}^2$ for iteration.

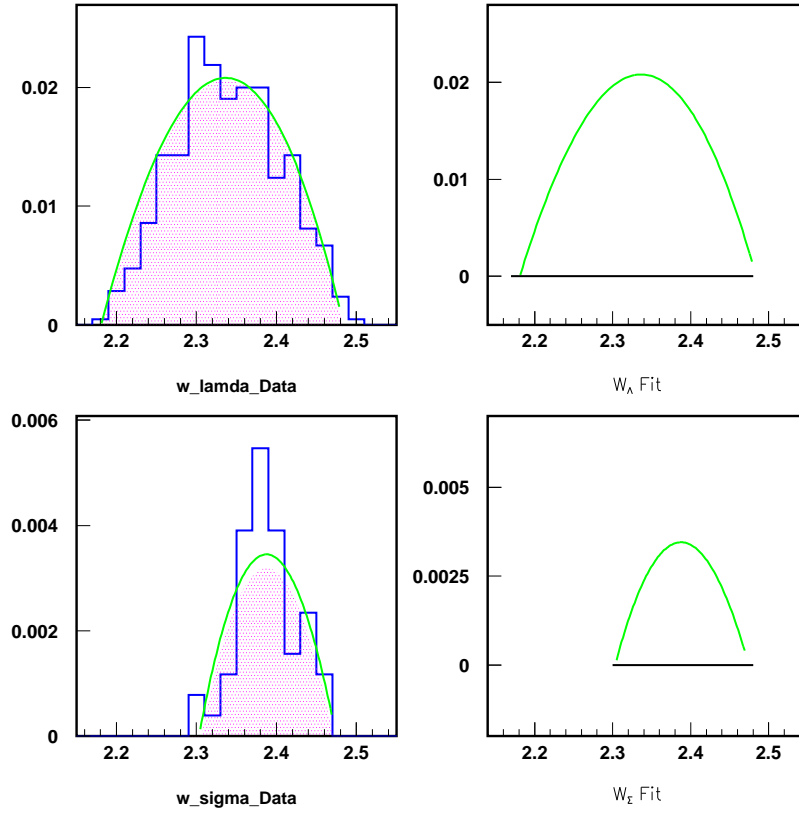


Figure B.7 Fitting the W data for kinematic settings of $Q^2=2.2 \text{ (GeV/c)}^2$ for iteration.

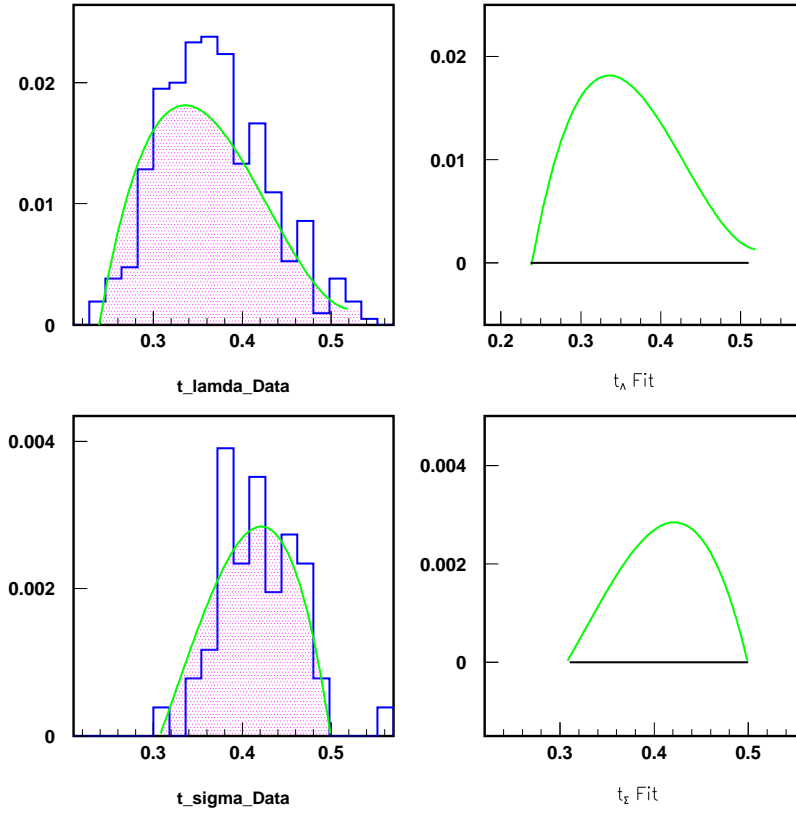


Figure B.8 Fitting the t data for kinematic settings of $Q^2=2.2 \text{ (GeV/c)}^2$ for iteration.